AD

QUANTITATIVE STRAIN AND STRESS DETERMINATION FROM HOLOGRAPHIC INTERFEROGRAMS

Final Technical Report

by

R. Dändliker, B. Ineichen, B. Eliasson, J. Mastner

September 1977

U.S. ARMY EUROPEAN RESEARCH OFFICE

and

U.S. AIR FORCE EUROPEAN OFFICE OF AEROSPACE RESEARCH

AND DEVELOPMENT

London England

Brown Boveri Research Center, CH-5405 Baden, Switzerland

SECURITY CLASSIFICATION OF THIS PAGE (When Data Entered)

REPORT DOCUMENTATION PAGE		READ INSTRUCTIONS BEFORE COMPLETING FORM
1. REPORT NUMBER	2. GOVT ACCESSION NO.	3. RECIPIENT'S CATALOG NUMBER
4. TITLE (and Subtitle) QUANTITATIVE STRAIN AND STRESS DETERMINATION FROM HOLOGRAPHIC INTERFEROGRAMS		5. TYPE OF REPORT & PERIOD COVERED FINAL TECHNICAL REPORT. 31 JAN 77 - SEP 77
		6. PERFORMING ORG. REPORT NUMBER
7. AUTHOR(s) R. DANDLIKER, B. INEICHEN, B. ELIASSON, J. MASTNER		8. CONTRACT OR GRANT NUMBER(s) DAERO-76-G-059
9. PERFORMING ORGANIZATION NAME AND ADDRESS BROWN, BOVERI RESEARCH CENTER CH-5405 BADEN, SWITZERLAND		10. PROGRAM ELEMENT, PROJECT, TASK AREA & WORK UNIT NUMBERS 6-11-02A-1T161102BH57-06-000
11. CONTROLLING OFFICE NAME AND ADDRESS US ARMY R&S GP (EUR) BOX 65, FPO NY 09510		12. REPORT DATE SEPTEMBER 1977
		13. NUMBER OF PAGES 47
14. MONITORING AGENCY NAME & ADDRESS(if different from Controlling Office) 50p.		15. SECURITY CLASS. (of this report) UNCLASSIFIED
		15a. DECLASSIFICATION/DOWNGRADING SCHEDULE

16. DISTRIBUTION STATEMENT (of this Report)

APPROVED FOR PUBLIC RELEASE; DISTRIBUTION UNLIMITED

17. DISTRIBUTION STATEMENT (of the abstract entered in Block 20, if different from Report)

18. SUPPLEMENTARY NOTES

19. KEY WORDS (Continue on reverse side if necessary and identify by block number)

(U) SURFACE STRAIN: (U) STRAIN: (U) STRESS: (U) HOLOGRAPHIC: (U) INTERFERENCE: (U) HOLOGRAMS: (U) INTERFEROMETRY

20. ABSTRACT (Continue on reverse side if necessary and identify by block number)

The basic problems of quantitative determination of mechanical strain through holographic interferometry are discussed. A solution based on the calculation of local derivatives of the holographically recorded surface displacements is described. This method uses essentially heterodyne holographic interferometry for the quantitative determination of the surface displacement from the fringe pattern in the image plane. With this techniques the interference phase can be measured with an accuracy and

DD FORM 1473 1 JAN 73   EDITION OF 1 NOV 65 IS OBSOLETE   UNCLASSIFIED

SECURITY CLASSIFICATION OF THIS PAGE (When Data Entered)

$+or-$ deg   .001.

and reproducibility of $\pm 0.3^{\circ}$ at any point in the fringe pattern, corresponding to an interpolation of better than 10^{-3} of one fringe. Numerical examples are given for the sensitivity and accuracy of surface strain measurements and the determination of bending and torsion. Experimental results for bending and torsion of arbitrarily curved and twisted space beams, such as turbine blades, are reported. Accuracy and agreement with theory are within a few percent.

ACCESSION for

NTIS	White Section
DDC	B ff Section ☐
UNANNOUNCED	☐
JUSTIFICATION	

BY

DISTRIBUTION/AVAILABILITY CODES

SPECIAL

A

QUANTITATIVE STRAIN AND STRESS DETERMINATION FROM HOLOGRAPHIC
INTERFEROGRAMS

Final Technical Report

by

R. Dändliker, B. Ineichen, B. Eliasson, J. Mastner

September 1977

U.S. ARMY EUROPEAN RESEARCH OFFICE

and

U.S. AIR FORCE EUROPEAN OFFICE OF AEROSPACE RESEARCH

AND DEVELOPMENT

London England

GRANT NUMBER DA-ERO-76-G-059

Brown Boveri Research Center, CH-5405 Baden, Switzerland

Summary

The basic problems of quantitative determination of mechanical strain through holographic interferometry are discussed. A solution based on the calculation of local derivatives of the holographically recorded surface displacements is described. This method uses essentially heterodyne holographic interferometry for the quantitative determination of the surface displacement from the fringe pattern in the image plane. With this technique the interference phase can be measured with an accuracy and reproducibility of $\pm 0.3^{\circ}$ at any point in the fringe pattern, corresponding to an interpolation of better than 10^{-3} of one fringe. Numerical examples are given for the sensitivity and accuracy of surface strain measurements and the determination of bending and torsion. Experimental results for bending and torsion of arbitrarily curved and twisted space beams, such as turbine blades, are reported. Accuracy and agreement with theory are within a few percent.

Contents

List of Illustrations

1. Introduction

The general objectives of the research program have been theoretical and experimental investigations of methods for the quantitative determination of surface strain and stress of mechanical parts from holographic interferometry. This includes the development of analytical and numerical methods to calculate the surface strain from the object deformation as well as development of special opto-electronic systems to increase the sensitivity and the accuracy for the evaluation and interpolation of holographic interference patterns.

Many forms of holographic interferometry are known for mechanical deformation or vibration analysis[1]. A common feature of all these methods is that the interferometric information is presented in the form of interference fringes in the image of the object under investigation. In case of mechanical deformation and vibration studies it is known that the relevant strain and stress values are given by first or second order derivatives of the interferometrically measured surface displacement[2,3]. Therefore the quantitative determination of the local strain parameters is only possible if the accuracy of the evaluation of holographic interferograms is increased drastically beyond the simple technique of counting fringe orders.

To solve this problem a basically new approach for the quantitative evaluation of holographic interferograms is considered. *Heterodyne holographic interferometry*[4,5] increases the accuracy by at least a factor 100.

Moreover the quantitative determination of mechanical strain on the surface of an arbitrarily shaped object through holographic interferometry requires the knowledge of the *relation between surface strain and surface displacement* and the *relation between derivatives of the surface displacement and the interference fringes in the image plane*. This relations have been established theoretically and are used to develop corresponding numerical programs to evaluate strain, stress, bending and torsion from holographic interferometry.

2. Heterodyne Holographic Interferometry

Holographic interferometry is a powerful tool to determine surface displacement fields of solid objects. The relevant information is the phase difference ϕ between the two optical wave fields corresponding to the two object states before and after deformation. These phase differences show up as intensity variation, the so-called interference fringes, in the image of the objects. However, quantitative information on the interference phase can only be obtained reliably from the maxima and minima of the interference fringes, corresponding to multiples of 180° or π in the phase ϕ. Any interpolation between the fringes is difficult and not very accurate. Heterodyne holographic interferometry is a new optoelectronic technique which overcomes this limitation and allows to determine the interference phase at any position within the fringe pattern with an accuracy of better than 0.4° or 1/1000 of a fringe[4,5].

2.1. Heterodyne Interferometry

The basic idea of heterodyne interfeometry is to introduce a small frequency shift between the optical frequencies of the two interfering light fields. This results in an intensity modulation at the beat frequency of the two light fields for any given point of the interference pattern. The optical phase difference is converted into the phase of the beat frequency[6,7].

The two light fields are then described by their complex amplitudes

$$V_1(\vec{x}, t) = a_1(\vec{x}) \exp i\left[\omega_1 t + \phi_1(\vec{x})\right],$$

$$V_2(\vec{x}, t) = a_2(\vec{x}) \exp i\left[\omega_2 t + \phi_2(\vec{x})\right],$$

(2.1)

where $a_{1,2}$ are the real amplitudes, $\phi_{1,2}$ the phases, and $\omega_{1,2}$ the optical frequencies.

A photodetector placed at the point $P(\vec{x})$ in the superposition of these two light fields sees the time dependent intensity

$$I(\vec{x},t) = |V_1+V_2|^2 = a_1^2(\vec{x})+a_2^2(\vec{x})+2a_1(\vec{x})a_2(\vec{x})\cos\left[(\omega_1-\omega_2)t+\phi_1(\vec{x})-\phi_2(\vec{x})\right]$$

$$= a_1^2(\vec{x})+a_2^2(\vec{x})+2a_1(\vec{x})\vec{a}_2(\vec{x})\cos\left[\Omega t+\phi(\vec{x})\right]. \tag{2.2}$$

Equation (2.2) shows that the interference phase $\phi(\vec{x}) = \phi_1(\vec{x})-\phi_2(\vec{x})$, i.e. the optical phase difference between the two light fields, appears as the phase of the intensity modulation at the beat frequency $\Omega = \omega_1-\omega_2$.

As long as Ω is small enough to be resolved by a photodetector, this modulation can be separated by an electronic filter centered at Ω and the phase can be measured electrically with respect to a reference signal at the same frequency. As will be described in Section 2.3. the interference phase can be measured essentially independent of the amplitude of the modulated signal and therefore also independent of the amplitudes $a_1(\vec{x})$ and $a_2(\vec{x})$ of the interfering light fields. The accuracy for the electronic phase measurement can easily be better than 1° or $2\Pi/400$. Techniques and experimental realizations for the frequency shift will also be given in Section 2.3.

The heterodyne method can be applied, with some restrictions, to holographic interferometry:

- Application to real time holographic interferometry is straight forward
- Application to double exposure holographic interferometry is possible, of the two wavefields are stored independently in the hologram[4,8]. The most convenient solution with two different reference waves will be described in Section 2.2.
- Application to time average holographic interferometry is not possible, since the averaged wave field shows already frozen interference fringes.

It is instructive to compare heterodyne interferometry and classical fringe intensity detection with respect to the accuracy of interference phase measurement. First of all it should be pointed out that in case of intensity detection the interference phase can only be reliably deduced from the position of the fringe maxima and the fringe minima, because any intermediate value of the intensity depends on both phase and average intensity, which is in general not constant across the image of the object. The heterodyne interferometry overcomes this limitation, since phase and amplitude of the interference term can be separated electronically and the fringes travel across the image so that the sensitivity and accuracy is the same at any position. This difference is visualized in Fig. 2.1: *From the interference pattern only the positions X_i of the fringe maxima and minima $\phi_i = m\pi$ are obtained; from heterodyne interferometry the actual interference phase ϕ_n is obtained at any desired position x_n.*

2.2. Two-reference-beam Holographic Interferometry

Double exposure holographic interferometry probably is the most common and convenient kind of holographic interferometry. It is therefore very important to find a solution to use the described heterodyne method together with double exposure holographic interferometry. This is possible if the two wavefields are stored independently in the hologram, so that during reconstruction the different frequencies for the two interfering light fields can be introduced by using two reference waves of different frequencies. The most convenient realization is to use two different reference waves for that purpose[4,8].

Multiple-reference-beam holography has been proposed and applied by various researchers for inspecting phase objects, holographic recording of polarization, or as means for introducing flexibility into conventional double exposed holograms. Indeed, if each image has its own reconstruction beam, one has access to each image separately, as well as to their mutual interference pattern. A

double-exposure double-reference-beam holographic setup, as shown in Fig. 2.2, is basically a superposition of two independent holograms of the same, but deformed, object on the same hologram plate.

The hologram $H(\vec{x})$, which is the interference of reference and object waves in the hologram plane (x,y), consists in this case of

$$H(\vec{x}) = R_1 O_1^* + R_1^* O_1 + R_2 O_2^* + R_2^* O_2, \qquad (2.3)$$

where R_1 and R_2 are the two different reference waves used to record O_1 and O_2, respectively.

Upon illumination of the hologram with the two reference beams R_1 and R_2 eight terms result from the product of $R_1 + R_2$ with $H(\vec{x})$.[9] As shown in Fig. 2.3, two pairs of reconstructions, viz. $R_1 R_1^* O_1$, $R_2 R_2^* O_2$ and $R_2 R_1 O_1^*$, $R_1 R_2 O_2^*$, will be in exact register giving rise to interference. The images $R_1 R_1^* O_1$, $R_2 R_2^* O_2$ and $R_1 R_1 O_1^*$, $R_2 R_2 O_2^*$ are the primary and conjugate self-reconstructions, respectively, of the two independent holograms with their own reference waves. In addition, $R_2 R_1^* O_1$, $R_1 R_2^* O_2$ and $R_2 R_1 O_1^*$, $R_1 R_2 O_2^*$ are the primary and conjugate cross-reconstruction, respectively, of the two holograms with the wrong reference waves.

The locations of the reconstructed images depend on the mutual position of the reference waves and the object during recording. For the experimental demonstration of the various reconstructions and their respective location in Fig. 2.3 the reference sources were approximately at the same distance from the hologram as the object. Therefore, following Eq. (2) in Ref. 8 all reconstructed images are virtual and appear focused at nearly the same distance behind the hologram as the original object. For reasons of aberrations it is recommended to work exclusively with the interfering pair of primary, self-reconstructed waves $R_1 R_1^* O_1$ and $R_2 R_2^* O_2$.

The directions of propagation of various reconstructed waves can also be constructed and visualized with the help of a sphere of radius k in the k-space where each propagation vector is represented by a point on that sphere. For the example scetched in Fig. 2.4 the object vectors $\vec{k}_{01}$ and $\vec{k}_{02}$ have been chosen along the z direction, i.e. normal to the hologram plane. The optimum choice of the reference sources to avoid disturbing overlapping of the different reconstructions can be deduced from Fig. 2.4. Symmetrically positioned reference beams with respect to the object location are not recommended, since for this case the two pairs of interfering images will be reconstructed along the same propagation direction. The best choice is to have both reference sources at the same side of the object with a mutual separation as small as possible. This means that the angular spacing between the two reference waves should be just larger than the angular size of the object in the corresponding direction, so that the reconstructions $R_1 R_1^* O_1$, $R_2 R_2^* O_2$ and $R_2 R_1 O_1^*$, $R_1 R_2 O_2^*$ carrying interference information are mutually separated and do not overlap with $R_2 R_1^* O_1$ nor $R_1 R_2^* O_2$.

Two-reference-beam holographic interferometry is expected to be sensitive to repositioning errors for the reconstruction process because misalignments of hologram and reference waves will not affect both reconstructed waves in the same manner. Angular misalignment of both hologram plate or reference waves causes mainly an additional linear phase deviation across the hologram between the reconstructed wave fields[9]. The effect of these linear phase deviations on the image of the object, obtained by a lens in the reconstructed wave field, can be simulated by a wedge positioned at the hologram plane affecting only one of the reconstructions. The corresponding schematical arrangement is shown in Fig. 2.5.

The effect of this wedge on the image can be calculated using the Fresnel approximation for the stepwise propagation of the light field from plane to plane. The result is both a linear phase dis-

tortion $\psi_o(x_1)$ across the object and a virtual transverse displacement u_o' of the object. The relations to the phase deviation $\psi_H(x_2)$ in the hologram plane are found to be[9]

$$\psi_H(x_2) = k\alpha x_2, \quad \psi_o(x_1) = [k\alpha b/(a+b)]x_1, \quad u_o' = \alpha a. \tag{2.4}$$

For holographic interferometry the phase distortion $\psi_o(x_1)$ across the object is dangerous because it changes the interference pattern, whereas a lateral shift u_o' does only reduce the fringe contrast. Fortunately the phase distortion can be nearly eliminated by placing the lens as close as possible to the hologram, so that $b/(a+b) \ll 1$. In this case the lateral shift is approximately $u_o' = \alpha d_o$.

An analysis of the phase deviation introduced by different kinds of misalignment shows that for plane or quasi plane reference waves only rotations of the hologram plate and a change of the mutual angle between the two reference waves are important[9]. The phase deviation in the hologram plane (x,y) due to rotations, is given by

$$\psi_H(\vec{x}) = \vec{k}_1\Delta\vec{x} - \vec{k}_2\Delta\vec{x} = (\vec{k}_1-\vec{k}_2)(\vec{w} \times \vec{x}_H) \tag{2.5}$$

where $\vec{k}_1$ and $\vec{k}_2$ are wavevectors of the two reference waves, $\Delta\vec{x} = (\Delta x,\Delta y)$ is the change of coordinates due to the rotation $\vec{w} = (\Delta\alpha,\Delta\beta,\Delta\gamma)$, and $\vec{x}_H = (x,y)$ are coordinates in the hologram plane. It is seen that the phase deviation depends only on the difference $\Delta\vec{k} = (\vec{k}_1-\vec{k}_2)$ of the two wavevectors and does vanish for identical reference waves, which is the case in classical double exposure holography. The maximum slope of the phase deviation is obtained from Eq. (2.5) as

$$\alpha = \left[(\Delta k_y\Delta\gamma - k_z\Delta\beta)^2 + (\Delta k_z\Delta\alpha - \Delta k_x\Delta\gamma)^2\right]^{1/2}, \tag{2.6}$$

where the z-axis is assumed to be normal to the hologram surface and $\Delta\alpha$, $\Delta\beta$, $\Delta\gamma$ are the angular rotations around the x,y,z-axis,

respectively. With a partially symmetric choice of the reference waves one can obtain $\Delta k_z = 0$, so that the rotation $\Delta \gamma$ around the normal to the hologram plate remains as the only essential contribution to the phase deviation. A change $\Delta \delta$ of the mutual angle δ between the two reference waves produces a phase difference

$$\psi_H(\vec{x}_H) = \frac{(\vec{k}_1 - \vec{k}_2)}{|\vec{k}_1 - \vec{k}_2|} \vec{x}_H \Delta \delta, \tag{2.7}$$

which yields a maximum slope of

$$\alpha = (\Delta k_x^2 + \Delta k_y^2)^{1/2} (\Delta k_x^2 + \Delta k_y^2 + \Delta k_z^2)^{-1/2} \Delta \delta . \tag{2.8}$$

In any case the alignment requirements are considerably less stringent than in real-time holography. If the same experimental setup is used for recording and reconstruction, usually only a slight readjustment of the rotational position of the hologram plate as can be deduced from Eq. (2.6) is necessary to get minimum or zero fringes across the hologram and at the same time maximum fringe contrast in the image.

Two-reference-beam holographic interferometry is applied in the following way to realize the heterodyne method for double exposure holographic interferometry (see Fig. 2.2): The first object state O_1 is recorded using beam R_1 as a reference. A stop is placed in beam R_2 so that it does not illuminate the hologram plate. The second object state O_2 is recorded in the same manner, except that beam R_2 is used as a reference and beam R_1 is stopped. All light fields during recording have the same optical frequency ω_R. After processing the hologram is reconstructed with geometrically identical reference waves R_1 and R_2, but of slightly different optical frequencies ω_1 and ω_2, respectively. The reconstructed wave fields O_1 and O_2 have the same frequencies as their respective reference waves. This meets precisely the conditions

necessary for heterodyne interferometry between these two re-
constructed wavefields. The frequency difference $\Omega = \omega_1 - \omega_2$ has
to be small enough to be resolved by photodetectors ($\Omega/2\pi < 100$ MHz).
The relative frequency change $\Omega/\omega_{1,2}$ is therefore smaller than
2×10^{-7} for visible light. The resulting changes in the propagation
of the light waves are thus very much below any optical resolution.

2.3. Experimental Realization and Results

Besides the standard holographic technique and equipment one needs
for heterodyne holographic interferometry also methods to generate
the desired frequency offset Ω, to detect the modulated signals,
and to measure their phase accurately. For small frequency off-
sets ($\Omega < 2\pi \times 1$ kHz) a mechanically rotating $\lambda/2$-plate and sub-
sequent polarizing elements can be used as in the early experiments
of heterodyne interferometry[6]. For the sake of stability, accura-
cy, and measuring speed, however, larger frequency offsets
($\Omega \overset{\sim}{=} 2\pi \times 100$ kHz) are advisable. This can be realized adequately
only with either rotating radial gratings[10] or acousto-optical
modulators[11]. The disadvantage of the rotating radial grating
is the fixed intensity ratios between the different object and
reference beams, given by the diffraction efficiency of the gra-
ting, which does not allow to optimize the light economy for both
recording and reconstruction independently. Moreover, most rota-
ting radial gratings show residual amplitude modulation due to
grating imperfection which may disturb the phase measurement
eventually.

For the phase measurement one needs a signal to act as a reference.
Therefore at least two photodetectors are placed in the image of
the object under investigation. One detector may be at a fixed
position while the other scans the image, or both detectors may
be movable at a fixed relative mutual separation. The latter
measures rather fringe density or slope of the interference phase
function than the interference phase itself. Nevertheless it has

the advantage to be less sensitive to slight variations of the position of the detectors, as long as their mutual separation is kept constant, and to yield directly local derivatives, which are in case of displacement measurements related to the strain. The integral interference phase can be calculated sufficiently accurate by summation of the increments. Photomultiplier tubes rather than semiconductor photodiodes should be used as photodetectors because of their nearly noise free and phase distortion free high gain. The disadvantage of photomultiplier tubes to be bulky can be overcome by using fibre optics to collect the light in the image plane.

All electronic amplifiers and filters in the signal paths should be designed carefully to avoid phase distortion which could reduce the accuracy of the phase measurements. Especially narrow band filters for noise reduction should be avoided. A bandwidth of somewhat less than half the modulation frequency Ω is advisable to cut down the d.c. component and harmonics. The phase is measured either by a phase sensitive detector and a calibrated, variable phase shifter or more conveniently by a zero-crossing phasemeter. Both kinds of instruments are commercially available with resolution down to 0.1° for the phase. The zero-crossing phase meter requires for proper operation, i.e. to avoid multiple zero crossings, a signal-to-noise ratio of at least 20 dB and a noise bandwidth of less than the signal frequency. The signal noise introduces a phase error $\delta\phi$ due to the fluctuations of the zero-crossings. This phase error is found to be

$$\delta\phi = (SNR)^{-1/2} N^{-1/2} = (SNR)^{-1/2} (\tau/T)^{-1/2}, \qquad (2.9)$$

where $N = \tau/T$ is the number of zero crossings observed during the integration time τ of the phase meter. This means that a single measurement ($N = 1$) with SNR = 20 dB yields $\delta\phi = 6^{\circ}$. This is reduced to $\delta\phi = 0.06^{\circ}$ for $N = 10^{4}$ which corresponds for example to $\tau = 100$ ms for a frequency of 100 kHz ($T = 10$ μs).

The SNR of the detector signals can be estimated from the holographic setup, the hologram efficiency, and the laser power. In case of shot-noise limited detection with a photomultiplier the signal-to-noise ratio is found to be

$$SNR = P\gamma^2 \eta_H \eta_D A_D / 2A_o h\nu B,$$ (2.10)

where P = power of the reconstructing reference beams, γ = fringe contrast, η_H = hologram efficiency, η_D = quantum efficiency of the detector, A_D = detector area, A_o = area of reconstructed object in the image plane, $h\nu$ = photon energy, B = detection bandwidth. The power P of the reference beam is defined as the power falling on that area of the hologram, which contributes to the reconstructed image. An estimation for the following reasonable experimental parameters P = 5 mW, γ = 0.5, η_H = 0.1 (bleached hologram). η_D = 0.1, A_D = 7.8×10^{-6} m^2 (ϕ_D = 1 mm), A_o = 0.1 m^2, $h\nu$ = 3.8 10^{-19} Ws (λ = 0.514 nm), B = 10 kHz, yields a SNR of about 40 dB. Without taking special precautions to save light one needs about 20 times more laser output power, i.e. P_L = 100 mW in the above example, than actually used to reconstruct the image, due to the losses at the optical components and comparatively large spots of the reference beams on the hologram to get a uniform illumination.

Besides the phase error due to amplitude noise, as given in Eq. (2.9) and (2.10), additional phase fluctuations may occur in the signal. These are mainly caused by instabilities, e.g. in the path length if the two reference waves, and by mechanical instabilities of the position of detector and reconstructed image. The overall accuracy of phase measurement, including these phase fluctuations, has recently been investigated experimentally[12] for a special application. The first experimental verification of heterodyne holographic interferometry was made for pure bending of a cantilever[5]. The results indicated an accuracy of interference phase of $\delta\phi$ = 0.3^o, which corresponds to less than 1/1000 of a fringe.

A somewhat more advanced setup for heterodyne holographic inter-
ferometry is shown in Fig. 2.6. In this case the frequency shift
of $\Omega = 2\pi \times 100$ kHz is realized by two commercially available
acoustooptical modulators M_1 and M_2 in cascade to give opposite
frequency shift. During recording both modulators are driven with
40 MHz, so that the net shift is zero. During reconstruction
one modulator is driven with 40 MHz and the other one with 40.1 MHz
so that the net shift is the desired 100 kHz. An array of three
detectors is used to scan the image. The two differences $\Delta\phi_\xi$ and
$\Delta\phi_\eta$ in the orthogonal directions ξ and η are measured rather than
the interference phase $\phi(\xi,\eta)$ itself. The electronic equipment
for automatic measurement and data acquisition is shown in Fig. 2.7.
The driver for the two acoustooptical modulators (40 MHz and 40.1
MHz) is seen at the bottom. The three photomultipliers, D_1, D_2,
D_3 in Fig. 2.6, get their light from the detection points in the
image plane by optical fibre-bundles. In the center box the beat
frequency at 100 kHz is filtered out from the photomultiplier sig-
nals with a bandwidth of $B = 10$ kHz. The signal amplitudes are
kept approximately constant independent of the intensity across
the image by control of the photomultiplier voltage. The phase
differences $\Delta\phi_\xi$ and $\Delta\phi_\eta$ are measured with two zero-crossing phase-
meters, which interpolate the phase angle to 0.1° and count also
the multiples of 360°, which corresponds to the fringe number.
The detector array is mounted on a step-motor driven stage to scan
the image. The programmed scanning pattern is executed by the X-Y
control unit (top of Fig. 2.7). For any measured position the
ξ,η-coordinates as well as the interference phases are digitally
recorded on punch tape to be available for further data processing.
The measuring time for one position, including displacement and
data punch, is only a few seconds.

The overall accuracy of the phase measurement, including phase
fluctuations due to instabilities in the optical setup, are de-
termined experimentally. A double exposure, two-reference-beam

hologram of an object which has not been deformed between the
two exposures is recorded. The measured phase difference between
the signals of two detectors at a constant separation of 3 mm
is measured at different positions in the object image. The
result is shown in Fig. 2.8. The vertical bars indicate the
digital resolution of $\pm$ 0.05° of the phasemeter reading. The
measured phases show statistical variations with $\delta\phi = 0.22^{\circ}$
around an average value of $\phi = 1.05^{\circ}$. This means that the inter-
ference phase can indeed be measured with an accuracy of better than
$\delta\phi = 0.3^{\circ}$, corresponding to an interpolation of 10^{-3} of an inter-
ference fringe.

2.4. Discussion and Conclusions

It has been shown and experimentally verified that heterodyne
holography has the following outstanding properties:

- fringe interpolation to better than 10^{-3} of a fringe ($\delta\phi = \pm$ 0.3°),
- measurement with the same accuracy at any desired position in
  the image, therefore high spatial resolution (> 100 x 100 points)
- independent of brightness variations across the image,
- inherently direction sensitive, (i.e. increase and decrease of
  interference phase can be distinguished),
- computer readable output both for position and phase easily
  obtained (allows also on-line data-processing)

For these reasons heterodyne holographic interferometry is con-
sidered to be the most powerful technique to collect data for
quantitative measurement of surface displacement of solid objects.

Moreover, the heterodyne technique can be applied to nearly all
known kinds of holographic interferometry, except for time average
holograms. This list includes

- real time holographic interferometry: high temporal resolution,
  e.g. for vibration studies with an upper limit given by the
  frequency offset Ω; however the overall stability is expected
  to be smaller than for double exposure holography

- vibration analysis from multiple exposure holographic inter-
  ferometry recorded with stroboscopic illumination and syn-
  chroneous switching between the two reference beams

- depth contouring using dual illumination source or dual wave-
  length recording; by changing the angular position of the mode
  selection etalon of a single mode Ar-laser the frequency be-
  tween two exposures can be shifted by 6.7 GHz, yielding depth
  contours of about 22.5 mm separation and therefore 20 μm re-
  solution for $\delta\phi = 0.3^{\circ}$.

3. Quantitative Determination of Surface Displacement, Strain and Stress

In most practical applications of holographic interferometry to
solid objects rather the differential change of the surface dis-
placement, i.e. strain, tilt, bending, torsion, than the dis-
placement itself is of primary interest. In the following the
necessary theoretical relations between optics, geometry and me-
chanics will be worked out and illustrated with numerical and ex-
perimental examples.

3.1. Surface Displacement and Mechanical Deformation

The displacement of the object surface is completely described
by a vector $\vec{u}(x,y,z)$, where the coordinates x, y, and z are re-
stricted to the surface of the object, defined by a function

$$z = f(x,y), \text{ or } F(x,y,z) = z - f(x,y) = 0 . \tag{3.1}$$

If we suppose that the derivatives of the displacement are small
compared with unity, the vector gradient $\mu_{ik} = \text{grad } \vec{u}$ may be se-
parated additively in a symmetric part ε_{ik}, the strain, and a
skew-symmetric part Ω_{ik} the rotation[13],

$$\mu_{ik} = \text{grad } \vec{u} = \partial u_i/\partial x_k = \varepsilon_{ik} + \Omega_{ik},$$

$$\varepsilon_{ik} = \varepsilon_{ki} = \frac{1}{2} (\mu_{ik} + \mu_{ki}), \tag{3.2}$$

$$\Omega_{ik} = -\Omega_{ki} = \frac{1}{2} (\mu_{ik} - \mu_{ki}).$$

For elastic deformation of an isotropic material the relations between stress σ_{ik} and strain ε_{ik} is given by Hooke's law

$$\sigma_{ik} = \frac{E}{1+\nu} \left[\varepsilon_{ik} + \frac{\nu}{1-2\nu} \delta_{ik} (\varepsilon_{xx} + \varepsilon_{yy} + \varepsilon_{zz}) \right], \tag{3.3}$$

where E is the modulus of elasticity and ν is Poisson's ratio ($\delta_{ik} = 1$ for $i = k$ and $\delta_{ik} = 0$ for $i \neq k$).

For the discussion of the relations between surface displacement and surface strain it is appropriate to select the x,y,z coordinate system for the object point P so that the z-axis is parallel to the surface normal $\vec{n}$ and the x- and y-axis are parallel to the tangential plane (Fig. 3.1). From the observed surface displacement, however, it is not possible to determine grad $\vec{u} = \partial u_i/\partial x_k$ completely, because only the variations of $\vec{u}(x,y,z)$ along the surface $z = f(x,y)$ are accessible. This means, expressed in the special coordinate system shown in Fig. 3.1, that only the six components

$$\mu_{i\alpha} = \partial u_i/\partial x_\alpha$$

can be obtained, where here and the following greek indices (e.g. α, β) are used for in-plane components (u_x, u_y) and in-plane coordinates (x,y). The three remaining components

$$\mu_{iz} = \partial u_i/\partial z$$

have to be determined from additional relations. These relations
are obtained from the known mechanical boundary conditions at the
object surface[14]. They read

$$T_k = n_i \, \sigma_{ik} \qquad\qquad (3.4)$$

stating that the external forces T_k are in equilibrium to the
stress components normal to the surface. In most practical cases
the surface under observation is free of external forces ($T_k = 0$).
This implies $\sigma_{zi} = 0$, i.e. all normal stress components are zero,
and leads with Eqs. (3.2) and (3.3) to the 3 required additional
relations

$$\mu_{xz} = -\mu_{zx}, \quad \mu_{yz} = -\mu_{zy}. \quad \mu_{zz} = -\frac{\nu}{1-\nu} \, (\mu_{xx} + \mu_{yy}). \qquad (3.5)$$

With the Eqs. (3.2) and (3.5) the vector gradient of the surface
displacement $\mu_{ik} = \mathrm{grad} \, \vec{u}$ can be determined completely from the
observation of the displacement vector $\vec{u}$ on the surface. The com-
ponents of the rotation vector $\vec{\Omega}$ are explicitely

$$\Omega_x = \Omega_{zy} = \partial u_z/\partial y, \quad \Omega_y = \Omega_{xz} = -\partial u_z/\partial x, \quad \Omega_z = \Omega_{yx} = \frac{1}{2} \, (\partial u_y/\partial x - \partial u_x/\partial y).$$
$$(3.6)$$

Bending and torsion are given by the change of curvature of the
surface. The original curvature of the object surface is described
by a tensor κ with the elements

$$\kappa_{\alpha\beta} = \partial^2 f/\partial x_\alpha \partial x_\beta \qquad\qquad (3.7)$$

where $z = f(x,y)$ defines the surface and x_α are the orthogonal
coordinates (x,y) in the tangential plane[15] at the point P
(Fig. 3.1). Therefore the surface can be approximated around P
by the quadratic form

$$z = \frac{1}{2} \kappa_{\alpha\beta} x_\alpha x_\beta = \frac{1}{2} \kappa_{xx} x^2 + \kappa_{xy} xy + \frac{1}{2} \kappa_{yy} y^2. \tag{3.8}$$

The coordinates $\vec{x}' = (x',y',z')$ of the surface after displacement $\vec{u}$ are obtained from

$$\vec{x}' = \vec{x} + \vec{u}. \tag{3.9}$$

The displacement $\vec{u}$ is also expanded in a power series around the point P. To simplify the calculations any contribution of $\vec{u}$ corresponding to a rigid body motion rather than a deformation of the surface may be assumed to be zero, without loss of generality. This means that at the point P both the displacement $\vec{u}(P)$ and the rotation $\vec{\Omega}(P)$, as given in Eq. (3.6), vanish. Since Eq. (3.8) for the surface approximation is linear in z and quadratic in x and y the displacement component u_z is expanded up to quadratic terms while u_x and u_y are broken off after the linear terms. The coordinates of the surface after displacement read now

$$x' = x + (\partial u_x/\partial x) x + (\partial u_x/\partial y) y = (1 + \varepsilon_{xx}) x + \varepsilon_{xy} y$$

$$y' = y + (\partial u_y/\partial x) x + (\partial u_y/\partial y) y = (1 + \varepsilon_{yy}) y + \varepsilon_{xy} x \tag{3.10}$$

$$z' = z + \frac{1}{2} (\partial^2 u_z/\partial x^2) x^2 + (\partial^2 u_z/\partial x \partial y) xy + \frac{1}{2} (\partial^2 u_z/\partial y^2) y^2.$$

The change of curvature is obtained by introducing Eqs. (3.10) into the original quadratic form of the surface, as given in Eq. (3.8), and looking at the change of the coefficients in the new quadratic form afterwards. Restricting oneself to linear contributions in $\varepsilon_{\alpha\beta}$, since $\varepsilon_{\alpha\beta} \ll 1$, one gets finally the nice looking relations

$$\Delta\kappa_{\alpha\beta} = \kappa'_{\alpha\beta} - \kappa_{\alpha\beta} = \partial^2 u_z/\partial x_\alpha \partial x_\beta - \kappa_{\alpha\gamma} \varepsilon_{\gamma\beta} - \varepsilon_{\alpha\gamma} \kappa_{\gamma\beta}. \tag{3.11}$$

The change of curvature is seen to consist of two different contributions, namely the variation of the surface tilt $\partial^2 u_z/\partial x_\alpha \partial x_\beta$ and the influence of the surface strain $\varepsilon_{\alpha\beta}$, which reduces the appa-

rent curvature proportional to its original value $\kappa_{\alpha\beta}$. In the case of dominant bending and torsion the contributions of the second terms in Eq. (3.11) can be neglected, since the products of the curvature $\kappa_{\alpha\beta}$ and the strain $\varepsilon_{\alpha\beta}$ will be small. The bending (change of curvature) $\Delta\kappa_s$ and the torsion (rate of twist) $d\Omega_s/ds$ for an arbitrary direction $\vec{s}$ on the surface are obtained from $\Delta\kappa$ by the relations

$$\Delta\kappa_s = \Delta\kappa_{xx}\cos^2\theta + 2\Delta\kappa_{xy}\cos\theta\sin\theta + \Delta\kappa_{yy}\sin^2\theta,$$

$$d\Omega_s/ds = \Delta\kappa_{xy}\cos 2\theta + \frac{1}{2}(\Delta\kappa_{yy} - \Delta\kappa_{xx})\sin 2\theta,$$

(3.12)

where θ is the angle between the x-axis and the direction $\vec{s}$ (Fig. 3.1).

After that, all relations between surface displacement and mechanically relevant deformations are established. From Eqs. (3.2) and (3.11) it is seen that the in-plane strain $\varepsilon_{\alpha\beta}$ is obtained from the first derivatives of the in-plane displacement u_x, u_y, whereas the change of curvature $\Delta\kappa_{\alpha\beta}$ is mainly determined by the second derivatives of the out-of-plane displacement u_z.

3.2. Calculation of Displacement Vectors from Interference Fringes in the Image

The considered geometry of the setup for the holographic interferometry is shown in Fig. 3.2. It is assumed that the same imaging system is used for all the holographic interferograms with different sensitivity vectors $\vec{E}_n$. This can be realized using either different illumination source Q_n or different observation directions[16,17], e.g. different portions of the hologram and the lens aperture[18]. It has also been suggested to use entirely different views of the object to get the sensitivity vectors $\vec{E}_n$, but this is not recommended because of the different projections of the object formed in the images which makes proper position measurements and coordination of individual points on the surface quite

difficult and inaccurate. The actual observation point $P'(\xi',\eta')$ in the image plane is simply related to the point $P(\xi,\eta)$ in the conjugate object plane by the magnification. Therefore the (ξ,η,ζ) are used as image coordinates. The object coordinate system (x,y,z) for the corresponding point on the surface is mainly determined by the surface normal $\vec{n}$, as shown in Fig. 3.1.

The interference phase measured in the image is given by[16]

$$\phi_n(\xi,\eta) = (\vec{k}_Q - \vec{k}_A)_n \; \vec{u} = 2k \; (\vec{E}_n \vec{u}) = 2k \; U_n(\xi,\eta), \tag{3.14}$$

where $\vec{k}_Q$ and $\vec{k}_A$ are the wave vectors of the illumination and the observed light, respectively, and $U_n(\xi,\eta)$ is the appearant component of the displacement $\vec{u}$ in the direction of the sensitivity vector $\vec{E}_n(\xi,\eta)$. If the displacement vector is represented by its components $u'_k(\xi,\eta)$ in the image coordinate system (ξ,η,ζ), Eq. (3.14) can be written as

$$U_n(\xi,\eta) = e_{nk}(\xi,\eta) \; u'_k(\xi,\eta), \tag{3.15}$$

where e_{nk} are the components of the $\vec{E}_n(\xi,\eta)$ in the image system. Using three linearly independent sensitivity vectors Eq. (3.15) can be inverted to calculate the displacement components

$$u(\xi,\eta) = f_{kn}(\xi,\eta) \; U_n(\xi,\eta), \text{ with } f_{mn}e_{nk} = \delta_{mk}. \tag{3.16}$$

The elements $f_{kn}(\xi,\eta)$ of the inverse sensitivity matrix can be calculated either analytically or numerically from the recording and imaging geometry which determines the sensitivity vectors $\vec{E}_n(\xi,\eta)$.

The derivatives of the displacement $u'_k(\xi,\eta)$ in the image system are directly obtained from Eq. (3.16), taking into account that also the inverse sensitivity $f_{kn}(\xi,\eta)$ depends on the position in the image plane. In general the contributions of the differen-

tial change of the sensitivity vectors $E_n(\xi,\eta)$ cannot be neglected[14,17,19]. At least an estimation of these contributions is recommended in each special case. Therefore the derivatives in the image system read

$$\partial u_k'/\partial \xi_\alpha = f_{kn}(\partial U_n/\partial \xi_\alpha) + (\partial f_{nk}/\partial \xi_\alpha) U_n, \qquad (3.17a)$$

$$\partial^2 u_k'/\partial \xi_\alpha \partial \xi_\beta = f_{kn}(\partial^2 U_n/\partial \xi_\alpha \partial \xi_\beta) + (\partial f_{kn}/\partial \xi_\alpha)(\partial U_n/\partial \xi_\beta)$$

$$+ (\partial f_{kn}/\partial \xi_\beta)(\partial U_n/\partial \xi_\alpha) + (\partial^2 f_{kn}/\partial \xi_\alpha \partial \xi_\beta) U_n. \quad (3.17b)$$

More than three sensitivity vectors lead to an overdetermined equation system for $u_k'(\xi,\eta)$. One can take advantage of that to eliminate the zero fringe ambiguity[16] or to improve the accuracy by least-squares solutions of Eqs. (3.16) and (3.17). The zero fringe ambiguity is due to the fact that in general the absolute fringe order or interference phase cannot be determined from an interferogram unless the absolute value of the displacement is known for at least one object point accessible in the image. It has been shown that the determination of the absolute fringe order is always very inaccurate if the viewing directions are restricted to a relatively small solid angle by the limitations of the imaging optics or the hologram[20]. Therefore it is advisable to determine the absolute displacement just for one point of the object by some other techniques, e.g. using a second view of the object[20] or elastic connection to an undisplaced reference point. Since the absolute displacement appears in Eqs. (3.17) only in the correction terms with U_n, it has not to be determined very accurately for strain and bending measurements. Moreover one can try to reduce the differential change $(\partial f_{nk}/\partial \xi_\alpha)$ of the sensitivity vectors as much as possible, e.g. by plane wave illumination ($\vec{k}_Q$ = const.) and telecentric imaging ($\vec{k}_A$ = const.). However this complicates the holographic setup and limits the size of objects quite drastically.

The next step is to transform the displacement and its derivatives from the image system to the object system. For each point P the

relation between the image system (ξ, η, ζ) and the object system (x, y, z) can be described for that purpose approximately by a general rotation in space

$$x_m = R_{mk}\, \xi_k, \tag{3.18}$$

where R_{mk} is orthonormal, i.e. $R_{mk} R_{nk} = \delta_{mn}$. This approximation is valid as long as the distance between object surface and object plane (ξ, η) is small compared with the viewing distance. The rotation matrix R_{mk} is mainly determined by the direction of the surface normal

$$\vec{n}(P) = (n_\xi, n_\eta, n_\zeta), \text{ with } n_\xi^2 + n_\eta^2 + n_\zeta^2 = 1, \tag{3.19}$$

in the image system. If the orientation of the x-axis in the tangential plane is chosen so that it corresponds to the optical projection of the ξ-axis, i.e. in the (ξ, ζ) plane, the rotation matrix is explicitly given by

$$R_{mk} = \begin{bmatrix} n_\zeta/N & 0 & -n_\xi/N \\ -n_\xi n_\eta/N & N & -n_\eta n_\zeta/N \\ n_\xi & n_\eta & n_\zeta \end{bmatrix} \tag{3.20}$$

with $N = +\sqrt{1 - n_\eta^2}$. The inverse rotation matrix R_{km}^{-1} is simply obtained from $R_{km}^{-1} = R_{mk}$, since R_{mk} is orthonormal.

Using Eq. (3.18) the components of the displacement $\vec{u}$ in the object system are obtained by

$$u_m(x, y, z) = R_{mk} u_k'(\xi, \eta). \tag{3.21}$$

For the transformation of the derivatives, however, it has to be considered that the observed displacement $\vec{u}(x, y, z)$ is restricted to the surface defined by Eq. (3.1). Therefore one gets

$$\frac{\partial u_m}{\partial x_\alpha} = \frac{\partial u_m'}{\partial \xi_\beta} \left(\frac{\partial \xi_\beta}{\partial x_\alpha} + \frac{\partial \xi_\beta}{\partial z} \frac{\partial f}{\partial x_\alpha} \right) = \frac{\partial u_m'}{\partial \xi_\beta} (R_{\beta\alpha}^{-1} + R_{\beta z}^{-1} \frac{\partial f}{\partial x_\alpha}), \tag{3.22a}$$

$$\frac{\partial^2 u_m}{\partial x_\alpha \partial x_\beta} = \frac{\partial^2 u_m}{\partial \xi_\gamma \partial \xi_\delta} (R_{\gamma\alpha}^{-1} + R_{\gamma z}^{-1} \frac{\partial f}{\partial x_\alpha})(R_{\delta\beta}^{-1} + R_{\delta z}^{-1} \frac{\partial f}{\partial x_\alpha}) + \frac{\partial u_m'}{\partial \xi_\gamma} R_{\gamma z}^{-1} \frac{\partial^2 f}{\partial x_\alpha \partial x_\beta},$$

$$\tag{3.22b}$$

where the Eqs. (3.1) and (3.18) have been used. Because of the special choice of the object system at the observed point P (see Fig. 3.1), the derivatives of the surface are $\partial f / \partial x_\alpha = 0$ and $\partial^2 f / \partial x_\alpha \partial x_\beta = \kappa_{\alpha\beta}$, following the definition of curvature in Eq. (3.7) Finally the derivatives of the displacement in the object system can be calculated with

$$\partial u_m / \partial x_\alpha = R_{mk} (\partial u_k' / \partial \xi_\gamma) R_{\gamma\alpha}^{-1} \tag{3.23a}$$

$$\partial^2 u_m / \partial x_\alpha \partial x_\beta = R_{mk} (\partial^2 u_k' / \partial \xi_\gamma \partial \xi_\delta) R_{\gamma\alpha}^{-1} R_{\delta\beta}^{-1} + R_{mk} (\partial u_k' / \partial \xi_\gamma) R_{\gamma z}^{-1} \kappa_{\alpha\beta}. \tag{3.23b}$$

Remember that greek indices $(\alpha, \beta, \gamma, \delta)$ refer only to in-plane co-ordinates (x, y) or (ξ, η), respectively.

Surface strain ε_{ik} and rotation Ω_{ik} are obtained from the measured interference phase by consecutively applying Eqs. (3.14), (3.16), (3.17a), (3.23a) and (3.2) or (3.6). For the calculation of bending and torsion (change of curvature $\Delta\kappa$) Eqs. (3.17b), (3.23b) and (3.11) have to be used additionally.

3.3. Surface Strain Measurement

The sensitivity of the described method for the measurement of surface strain ε_{ik} using heterodyne holographic interferometry is estimated for the special case of three sensitivity vectors symmetrically distributed around the ζ-axis at the angle β and a simple rotation of the object system around the ξ-axis by the angle ϑ (Fig. 3.3). The sensitivity vectors and the rotation of the object system are then given by

$$
e_{nk} = \begin{bmatrix} \sin\beta & 0 & \cos\beta \\ -\sin\beta/2 & \sqrt{3}\,\sin\beta/2 & \cos\beta \\ -\sin\beta/2 & -\sqrt{3}\,\sin\beta/2 & \cos\beta \end{bmatrix} ; \quad R_{mk} = \begin{bmatrix} 1 & 0 & 0 \\ 0 & \cos\vartheta & \sin\vartheta \\ 0 & -\sin\vartheta & \cos\vartheta \end{bmatrix}
$$

$$(3.24)$$

Assuming that the errors of the phase measurements $\delta\phi$ are independent and equal for U_1, U_2 and U_3 the sensitivity $\delta\varepsilon$ for the strain components can be calculated versus the angles β and ϑ through Eqs. (3.2), (3.17a), and (3.23a). Neglecting the second terms for the differential change of the sensitivity in Eq. (3.17a) one gets

$$
\delta\varepsilon_{xx} = \sqrt{\frac{2}{3}}\,\frac{1}{\sin\beta}\,\frac{\delta U}{\Delta\xi}, \quad \delta\varepsilon_{xy} = \frac{1}{2}\sqrt{\frac{4\cos^2\vartheta}{3\sin^2\beta} + \frac{\sin^2\vartheta}{3\cos^2\beta}}\,\frac{\delta U}{\Delta\xi},
$$

$$
\delta\varepsilon_{yy} = \sqrt{\frac{2\cos^4\vartheta}{3\sin^2\beta} + \frac{\cos^2\vartheta\,\sin^2\vartheta}{3\cos^2\beta}}\,\frac{\delta U}{\Delta\xi}, \tag{3.25}
$$

where $\Delta\xi$ stands for the separation of the detectors either in ξ- or η-direction and $\delta U = 2k\delta\phi$ is the accuracy of the displacement measurement from the interference phase. Figure 3.3 shows numerical results of Eq. (3.25) for $\delta\phi = 0.4^\circ$, $\lambda = 514$ nm, and a spatial resolution of $\Delta\xi = \Delta\eta = 3$ mm in the image plane. The sensitivity $\delta\varepsilon$ for the different strain components and for different rotation angles ϑ of the surface normal are nearly the same. The main dependence is on the angle β between the sensitivity vectors $\vec{E}_n$ and the ζ-axis. A sensitivity of $\delta\varepsilon = 10^{-6} = 1$ μstrain is already obtained for $\beta = 5^\circ$, which can even be realized by observing the object through different portions of the same hologram.

The practical application of surface strain measurement with heterodyne holographic interferometry will be discussed for the example of a cylindrical tube with internal pressure as variable load.

A computer program has been developed for the numerical evaluation of the measured data, taking the object shape and the geometry of the optical setup into account. Experimental results, however, are not yet available, but the computer program has been tested with simulated data and the accuracy and sensitivity of the strain measurement are investigated and compared with the above estimation.

The test object is a cylindrical tube, closed at both ends, as shown in Fig. 3.4. Following Saint-Venant's principle the length is chosen large enough compared with the radius R to get undisturbed deformation at the center section of the tube. For a thin-walled tube (b<<R the stresses at the surface are found to be approximately[21)]

$$\sigma_x = pR/b, \qquad \sigma_y = pR/2b, \qquad \sigma_z = 0, \tag{3.26}$$

where p is the internal pressure. Using Hooke's law, as given in Eq. (3.3), one gets for the strain components

$$\varepsilon_x = \sigma_x(2-\nu)/2E, \quad \varepsilon_y = \sigma_x(1-2\nu)/2E, \quad \varepsilon_z = -\sigma_x(3\nu/2E). \tag{3.27}$$

From geometrical considerations the components of the displacement $\vec{u}(x,y,z)$ become then

$$u_x = 0, \quad u_y = u_o + \varepsilon_y y = u_o + \frac{1-2\nu}{2-\nu}\varepsilon_t y, \quad u_z = R\varepsilon_x = R\varepsilon_t, \tag{3.28}$$

where u_o is some bias displacement in the y-direction and the tangential strain ε_t has been introduced as the force parameter instead of the pressure p.

The optical geometry is shown in Fig. 3.5. Three divergent sources Q_1, Q_2, Q_3 are symmetrically distributed around the ζ-axis in the hologram plane and illuminate the object consecutively to record three two-reference-beam double-exposure holograms with different sensitivity vectors $\vec{E}_n$. The holograms are located at A, which is also the center of the lens aperture forming an image of the object

and its reconstructions in the image plane(ξ',η'). To insure that all three double-exposure holograms see the same object displacement it is recommended to record first the initial object state successively on all three holograms by their corresponding illumination sources Q_n and then, after deformation, recording the second object state in the same manner. It has been verified experimentally that for this purpose the three holograms can be recorded on the same plate mounted on a precision slide by shifting and repositioning the plate between the exposures. Thus the three holograms are accessible independently yielding the same image of the object but different fringe patterns. The numerical values for the parameters of the optical setup are as follows: image and object distance $d_1 = d_2 = 1.0$ m, separation of illumination from hologram center $q = 0.36$ m, outer diameter of the tube $2R = 0.2$ m.

The expected fringe pattern and the detector array in the image plane is shown in Fig. 3.6. The separations of the detectors are $\Delta\xi = \Delta\eta = 3$ mm. The simulated input data are calculated from a very crude approximation assuming constant sensitivity vectors for the entire object, as given by Eq. (3.24) for $\beta = 10^{\circ}$, which is only true for $\xi = \eta = 0$.

The expected phase differences $\Delta_\xi \phi_n$ and $\Delta_\eta \phi_n$ measured with the detector array are tabulated in Fig. 3.6 for two positions and the three sensitivity vectors $\vec{E}_n$. Also given are the absolute phase values ϕ_{on}, which can not be directly obtained from the holograms, as discussed in Section 3.2. In the first position $\xi = \eta = 0$ mm the surface is parallel to the image plane while in the second position $\xi = 66.0$ mm, $\eta = 0$ mm the surface is inclined by about 45°.

The computer program for the evaluation of strain and stress at the surface follows essentially the outlines in Section 3.2. The input consists of three sets of information:

- object surface geometry,
- optical geometry for recording and reconstruction,
- measured data of interference phase and position in the image plane.

The object surface is specified by a number of surface points on selected cross-sections of the object in a suitably chosen coordinate system. In case of the tube this cross-sections are obviously chosen perpendicular to the cylinder axis. All intermediate points on the surface are obtained by quadratic interpolation which yields at the same time the direction of the surface normal $\vec{n}$ and the curvature κ if desired. The position and orientation of the object with respect to the image system is specified by the geometrically determined shift and rotation of the respective coordinate systems.

The optical geometry is defined by the coordinates of the illumination sources $Q_n(\xi, \eta, \zeta)$ and the observation points $A_n(\xi, \eta, \zeta)$ in the image system, the image and object distances d_1 and d_2, and the wavelength λ. Additional geometrical parameters are the separation $\Delta\xi$ and $\Delta\eta$ of the detectors in the array.

The data input from the measurement consists of the phase differences $\Delta_\xi\phi_n$ and $\Delta_\eta\phi_n$ for the three sensitivity vectors $\vec{E}_n$ collected during a scan in the image plane at the corresponding position $P_i'(\xi_i, \eta_i)$. The incremental steps during the scan are preferably chosen equal to the detector separation $\Delta\xi$ or $\Delta\eta$. For the starting point the absolute phase values ϕ_{on} should be known, either by additional measurements or at least by an estimation.

The program calculates the intersection of the line-of-sight from the image point $P'(\xi, \eta)$ through the center of the aperture A with the object surface to determine the corresponding surface point $P(\xi, \eta, \zeta)$. The sensitivity vectors, the inverse sensitivity matrix f_{nk}, its derivatives $\partial f_{nk}/\partial\xi_\alpha$, and the rotation matrix R_{mk} are calculated numerically for any point of observation to determine the derivatives of the displacement $\partial u_k/\partial x_\alpha$ on the object surface.

The final output consists of the components of the surface strain $\varepsilon_{\alpha\beta}$, the surface rotations Ω_k, and the corresponding coordinates on the object. The surface stress $\sigma_{\alpha\beta}$ can also be calculated for given values of the modulus of elasticity E and Poisson's ratio ν.

For the considered test object a tangential strain of $\varepsilon_t = 5 \times 10^{-5}$ and the values $\nu = 0.34$ and $E = 7.26 \times 10^{10}$ Nm^{-2} for aluminium have been assumed. This yields, following Eqs. (3.26) and (3.27) theoretical surface strain and stress values of

$$\varepsilon_{\alpha\beta} = \begin{bmatrix} 5.00 \times 10^{-5} & 0.0 \\ 0.0 & 9.65 \times 10^{-6} \end{bmatrix} ; \quad \sigma_{\alpha\beta} = \begin{bmatrix} 4.37 \times 10^{6} & 0.0 \\ 0.0 & 2.19 \times 10^{6} \end{bmatrix} \text{Nm}^{-2}$$

independent on the position. These stresses correspond, for a wall thickness of $b = 3$ mm, to an internal pressure of $p = 1.31 \times 10^{5}$ $\text{Nm}^{-2} = 1.43$ at.

The computer results for the simulated input data given in Fig. 3.6 are for

$\xi = 0$ mm, $\eta = 0$ mm: $\qquad\qquad$ $\xi = 66$ mm, $\eta = 0$ mm:

$$\varepsilon_{\alpha\beta} = \begin{bmatrix} 4.56 \times 10^{-5} & -5.32 \times 10^{-10} \\ -5.32 \times 10^{-10} & 5.22 \times 10^{-6} \end{bmatrix} , \quad \varepsilon_{\alpha\beta} = \begin{bmatrix} 3.72 \times 10^{-5} & 3.13 \times 10^{-9} \\ 3.13 \times 10^{-9} & 5.66 \times 10^{-6} \end{bmatrix} .$$

The deviations between theory and computer results are mainly due to the approximation of constant sensitivity vectors made for the calculation of the simulated input data, whereas the numerical evaluation takes the effective geometrical variations of e_{nk} and f_{nk} into account. This fact is illustrated by comparison of the two terms for the derivative $\partial u_k'/\partial \xi_\alpha$ in Eq. (3.17a). For $\xi = \eta = 0$ one finds

$$\partial u_\xi'/\partial \xi = 5.00 \times 10^{-5} - 4.42 \times 10^{-6}, \quad \partial u_\eta'/\partial \eta = 9.64 \times 10^{-6} - 4.42 \times 10^{-6},$$

which shows clearly that the second contributions due to the differential change of the sensitivity vectors $\vec{E}_n$ are not always negligible. However, this result also indicates that an accuracy for the absolute phase of about $\delta \phi_{on} = 360^{\circ}$ (one fringe) would be sufficient to give an error of less than 3×10^{-7} for $\varepsilon_{\alpha\beta}$.

Furthermore the computer program has been used to investigate the influence of the geometrical parameters on the accuracy of the strain measurement. Independent deviations of the coordinates of the illumination sources Q_n and the object distance d_2 by 10% of their initial values have been assumed. It should be noted that these errors mean displacements of more than 30 mm, which is certainly exaggerated. The resulting relative rms error of the strain with respect to its maximum value $|\varepsilon|$ is found to be for

$\xi = 0$ mm, $\eta = 0$ mm: $\xi = 66$ mm, $\eta = 0$ mm:

$$\frac{\Delta \varepsilon}{|\varepsilon|} = \begin{bmatrix} 12.2\% & 2.1\% \\ 2.1\% & 2.9\% \end{bmatrix} \quad , \quad \frac{\Delta \varepsilon}{|\varepsilon|} = \begin{bmatrix} 5.1\% & 2.5\% \\ 2.5\% & 2.9\% \end{bmatrix} .$$

This shows clearly that the holographic surface strain measurement is not very sensitive to geometrical errors in the optical setup.

Finally the sensitivity has been tested by calculating the resulting strain for the minimum detectable phase differences $\delta\phi = 0.4^{\circ}$ as input, keeping $\phi_{on} = 0$ at the same time. The rms values for the surface strain at $\xi = \eta = 0$ ($\vartheta = 0^{\circ}$) and at the same position with the object tilted by $\vartheta = 45^{\circ}$ around the ξ-axis are found to be for

$\vartheta = 0^{\circ}$: $\vartheta = 45^{\circ}$:

$$\delta\varepsilon_{\alpha\beta} = \begin{bmatrix} 4.55\times10^{-7} & 3.21\times10^{-7} \\ 3.21\times10^{-7} & 4.54\times10^{-7} \end{bmatrix} \quad , \quad \delta\varepsilon_{\alpha\beta} = \begin{bmatrix} 4.53\times10^{-7} & 2.28\times10^{-7} \\ 2.28\times10^{-7} & 2.29\times10^{-7} \end{bmatrix}$$

These numerical results agree very well with the estimations of the sensitivity shown in Fig. 3.3 at $\beta = 10^{\circ}$, corresponding to the actu setup (Fig. 3.5).

The conclusion from these investigations is that one can determine with heterodyne holographic interferometry the local surface strain $\varepsilon_{\alpha\beta}$ with a sensitivity and accuracy of better than $\delta\varepsilon_{\alpha\beta} = 10^{-6} =$ 1 μstrain at a spatial resolution of 3 mm even for objects with a curved surface and an optical setup as shown in Fig. 3.5.

3.4. Pure Bending and Torsion

In the case of pure bending and torsion the change of curvature $\Delta\kappa$, as defined in Eq. (3.11), can be determined approximately using a single sensitivity vector $\vec{E}$.[14] Pure bending and torsion is characterized by the fact that a neutral line with zero strain exists inside the structure and that the strain increases linearly from the neutral line to the surface. Usually these structures are relatively thin, so that the surface is close to the neutral line and therefore the surface strain $\varepsilon_{\alpha\beta}$ is still small compared with the surface tilt, i.e. $\varepsilon_{\alpha\beta} << \Omega_x$, Ω_y. Moreover the differential change of the surface strain along the surface can be assumed to be negligibly small, which means that the line-element ds remains nearly constant. These assumptions allow to determine the change of curvature $\Delta\kappa$ from only one measured component $U = (\vec{u}\vec{E})$ of the displacement $\vec{u}$ in the direction of the sensitivity vector $\vec{E}$.

Following Eq. (3.11) in the case of negligible in-plane strain $(\varepsilon_{\alpha\beta}\kappa_{\gamma\beta} = 0)$ the change of curvature is essentially given by

$$\Delta\kappa_{\alpha\beta} = \partial^2 u_z/\partial x_\alpha \partial x_\beta.$$

(3.29)

Therefore one expects to obtain the $\Delta\kappa_{\alpha\beta}$ from the second derivative of the observed displacement

$$\frac{\partial U}{\partial x_\alpha \partial x_\beta} = \frac{\partial^2 u_k}{\partial x_\alpha \partial x_\beta} e_k + \frac{\partial u_k}{\partial x_\alpha}\frac{\partial e_k}{\partial x_\beta} + \frac{\partial u_k}{\partial x_\beta}\frac{\partial e_k}{\partial x_\alpha} + u_k \frac{\partial^2 e_k}{\partial x_\alpha \partial x_\beta},$$

(3.30)

where e_k are the components of the sensitivity vector $\vec{E}$ in the (x,y,z) coordinate system. The calculation of the change of surface strain $\varepsilon_{\alpha\beta}$ along the surface requires special care, since the orientation of the surface will also change due to its initial curvature $\kappa_{\alpha\beta}$. The surface strain $\varepsilon_{\alpha\beta}$ is obtained following Eq. (3.2) from the in-plane components

$$\bar{\mu}_{ik} = (\delta_{im} - n_i n_m)\,\mu_{mk}$$

(3.31)

of the vector gradient $\mu_{mk} = \text{grad } \vec{u}$, where the n_k are the components of the surface normal. From Eq. (3.31) one gets

$$\frac{\partial \bar{\mu}_{ik}}{\partial x_\alpha} = - \frac{\partial n_i}{\partial x_\alpha} n_m \mu_{mk} - n_i \frac{\partial n_m}{\partial x_\alpha} \mu_{mk} + (\delta_{im} - n_i n_m) \frac{\partial \mu_{mk}}{\partial x_\alpha} \quad , \tag{3.32}$$

which reduces to the simple relation

$$\partial \bar{\mu}_{\gamma\beta}/\partial x_\alpha = \kappa_{\gamma\alpha} (\partial u_z/\partial x_\beta) + \partial^2 u_\gamma/\partial x_\alpha \partial x_\beta \quad , \tag{3.33}$$

due to $n_x = n_y = 0$ and the relation $\partial n_\gamma/\partial x_\alpha = -\kappa_{\gamma\alpha}$, obtained from $\vec{n} = \text{grad } F$ and the Eqs. (3.1) and (3.7). The assumption of negligible change of the surface strain corresponds to $\partial \bar{\mu}_{\gamma\beta}/\partial x_\alpha = 0$ and Eq. (3.33) allows therefore to calculate $\partial^2 u_\gamma/\partial x_\alpha \partial x_\beta$ from the tilt $\partial u_z/\partial x_\beta$. The other assumption of negligible surface strain with respect to tilt means $\partial u_z/\partial x_\beta >> \partial u_\alpha/\partial x_\beta$ and therefore also $\partial U/\partial x_\alpha \cong (\partial u_z/\partial x_\alpha) e_z$, at least as long as $e_z \geq e_x, e_y$ or the angle between $\vec{n}$ and $\vec{E}$ is not larger than 45°. The last term in Eq. (3.30) is a second order effect in geometry changes and thus negligible unless the absolute displacement u_k is extremely large. Finally, one gets from Eqs. (3.29) and (3.30) the approximation

$$\Delta\kappa_{\alpha\beta} = \frac{1}{e_z} \frac{\partial^2 U}{\partial x_\alpha \partial x_\beta} + \frac{1}{e_z^2} \kappa_{\alpha\beta} \frac{\partial U}{\partial x_\gamma} e_\gamma - \frac{1}{e_z^2} \left(\frac{\partial U}{\partial x_\beta} \frac{\partial e_z}{\partial x_\alpha} + \frac{\partial U}{\partial x_\alpha} \frac{\partial e_z}{\partial x_\beta} \right) \quad . \tag{3.}$$

The derivatives of U in the object system (x,y) are obtained from the corresponding derivatives in the image system (ξ,η) similarly as shown in Eqs. (3.23)

$$\frac{\partial U}{\partial x_\alpha} = \frac{\partial U}{\partial \xi_\gamma} R_{\gamma\alpha}^{-1}, \quad \frac{\partial^2 U}{\partial x_\alpha \partial x_\beta} = \frac{\partial^2 U}{\partial \xi_\gamma \partial \xi_\delta} R_{\gamma\alpha}^{-1} R_{\delta\beta}^{-1} + \frac{\partial U}{\partial \xi_\gamma} R_{\gamma z}^{-1} \kappa_{\alpha\beta}. \tag{3.35}$$

For practical purposes it is convenient to use an experimental setup with the illumination source Ω (Fig. 3.2) close to the imaging lens, i.e. illumination and observation directions nearly the same.

To reduce the contributions of the differential change of the sensitivity vector, the distance d_2 between lens and object should be large compared with the transverse extension of the objects (d_2/ξ_{max}, $d_2/\eta_{max} > 5$). Under this experimental conditions and for a rotation of the object system around the ξ-axis by the angle (Fig. 3.3) one obtains from Eqs. (3.34) and (3.35) the following simple explicite expressions:

$$\Delta\kappa_{xx} = (\partial^2 U/\partial\xi^2)/\cos\vartheta$$

$$\Delta\kappa_{xy} = (\partial^2 U/d\xi\partial\eta) - (\partial U/\partial\xi)\tan\vartheta/d_2 \qquad (3.36)$$

$$\Delta\kappa_{yy} = (\partial^2 U/\partial\eta^2)\cos\vartheta - 2(\partial U/\partial\eta)\sin\vartheta/d_2.$$

The two terms containing the original curvature $\kappa_{\alpha\beta}$ in Eqs. (3.34) and (3.35) compensate each other as long as the sensitivity and the imaging directions are close enough.

The sensitivity $\delta(\Delta\kappa)$ of this method can be estimated from Eqs. (3.36) for the same parameters as used to calculate $\delta\epsilon$ (Fig. 3.3), viz. $\delta\phi = 0.4^\circ$, $\Delta\xi = \Delta\eta = 3$ mm, $\lambda = 514$ nm. For $\vartheta = 0$ one gets $\delta(\Delta\kappa) = 5\times10^{-5}$ m^{-1}, which corresponds to a bending induced strain of $\epsilon_D = 5\times10^{-7} = 0.5$ µstrain on a surface at 10 mm from the neutral line.

The Eqs. (3.34), (3.35) have been applied experimentally to a number of mechanical structures subjected to pure bending and torsion[12,14,22]. Equations (3.36) turned out to be very useful for fast evaluation of experiments and to give quite accurate results for simple object geometries. In Fig. 3.7 experimental results are shown for a turbine blade under static bending load. The experimental setup was the same as shown in Figs. 2.6 and 2.7. The bending along the blade axis (Fig. 3.7a) shows good agreement with mechanical theory. Note that the spatial resolution of the measurement is about 3 mm and that local variations of the bending stiffness can be detected. The change of curvature $\Delta\kappa_s$ of the

cross-sections normal to the axis have been measured in two independent experiments. The results in Fig. 3.7b show the excellent reproducibility of the measurements within the expected limits. These results are not compared with theory, since the mechanical model used does not include the change of cross-section as a reaction on bending load. Further experimental results for a turbine blade under torsional load are shown in Fig. 3.8 as triangles. For historical reasons the torsion is called $d\theta/dz$, where z is the blade axis. There is again good agreement with mechanical theory, shown as circles. The estimated absolute accuracy of about $\pm 5\%$ for the torsion is rather limited by the uncertainty of the mechanical and geometrical parameters, such as load, magnification factor, detector separation, than by the interference phase measurement. This becomes also clear from results of reproducibility tests which indicated errors of less than 3% even for the smallest values of torsion[12].

4. Conclusions and Recommendations

It has been shown that heterodyne holographic interferometry is a powerful tool for fringe interpolation, which allows to determine local derivatives of the surface displacement with sufficient accuracy for strain measurements. This technique is very well suited for automatisation and electronic data processing, which makes also on-line computer evaluation possible. It turns out that with heterodyne holographic interferometry one can determine even with small angles between the different sensitivity vectors, i.e. from a single hologram recording, strain values as small as 1 µstra. In addition one can determine the local change of curvature, which is useful in case of pure bending and torsion.

An advanced optical and electronical system for heterodyne holographic interferometry has been realized and experimentally tested. The results did confirm the expected specifications. An improvement in flexibility and simplicity of the holographic recording could be obtained by using two references which are very close together. This would reduce the repositioning requirements but de-

crease the phase accuracy due to the overlapping of undesired reconstructions[22]. The performance of such a setup need further experimental investigations.

An addition to the successful experimental tests for pure bending and torsion and the computer simulations for surface strain evaluation in case of general deformations one should verify the latter case also experimentally, e.g. for the described cylindrical tube as test object.

Further applications of heterodyne holographic interferometry to vibration analysis would be certainly of great importance. Corresponding experimental investigations either with time resolved real-time holographic interferometry or with stroboscopic hologram recording are recommended to dertermine the capabilities of these new techniques.
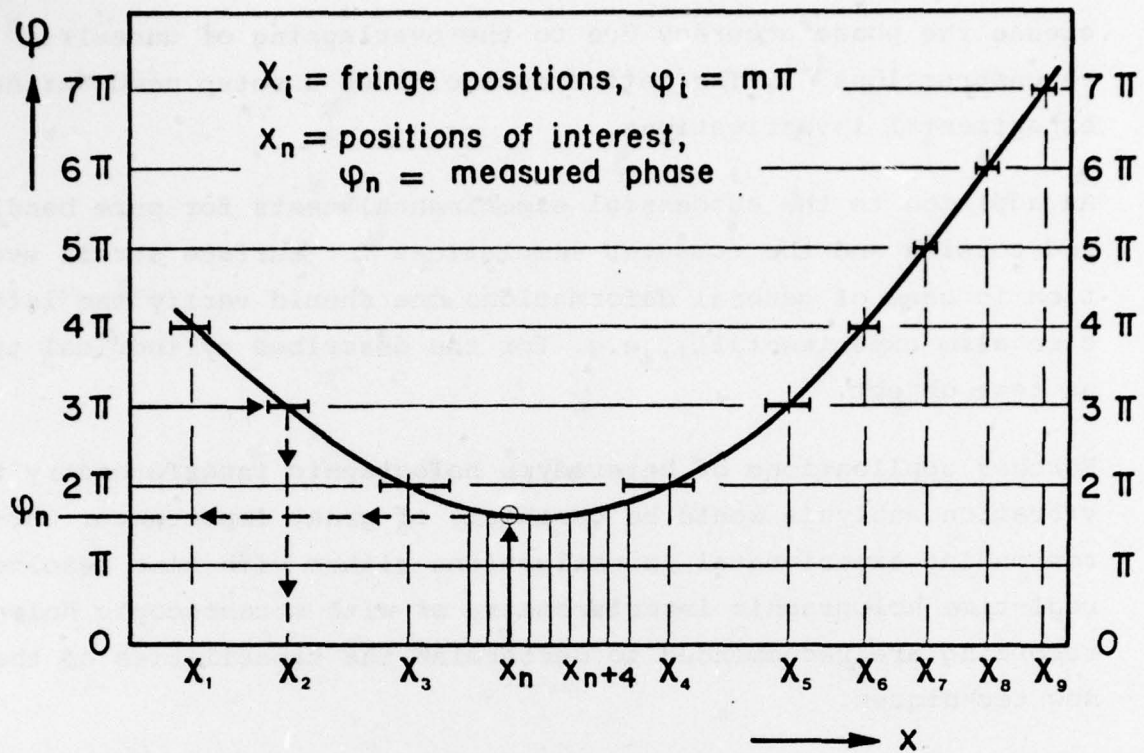
Fig. 2.1   Comparison of fringe counting and interference phase measurement.
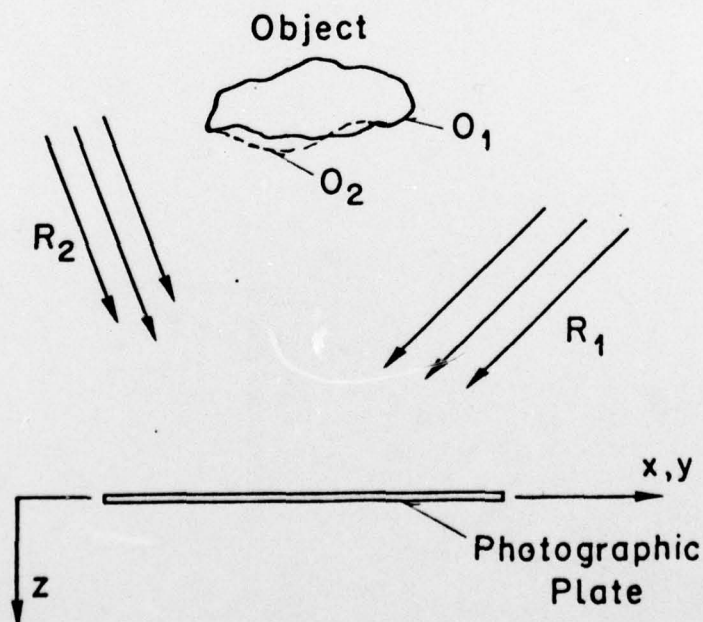
Fig. 2.2   Setup for recording double exposure holograms with two reference beams. R_1 and O_1 are used for the first exposure, while R_2 and O_2 are used for the second one.
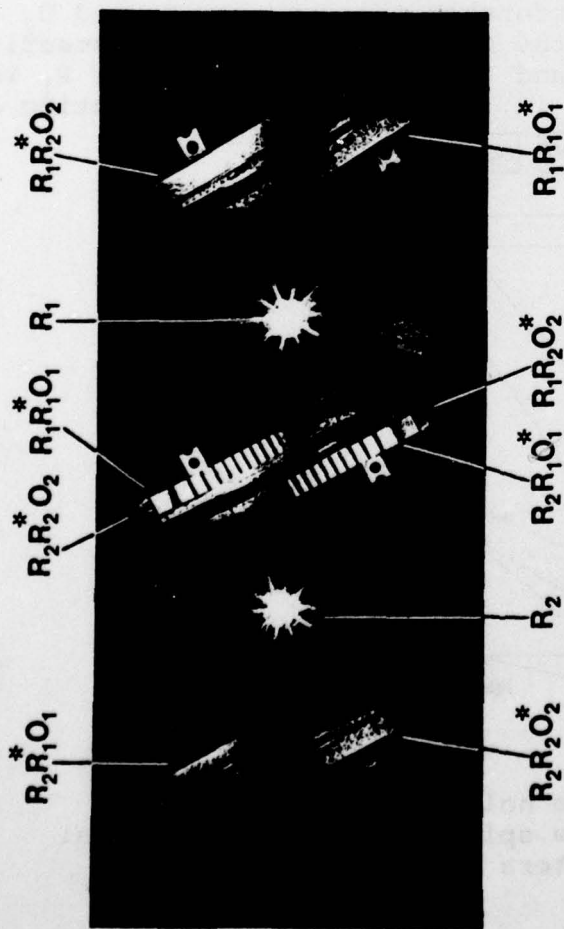
Fig. 2.3 Reconstructed images from a two-reference-beam holographic interferometry setup.
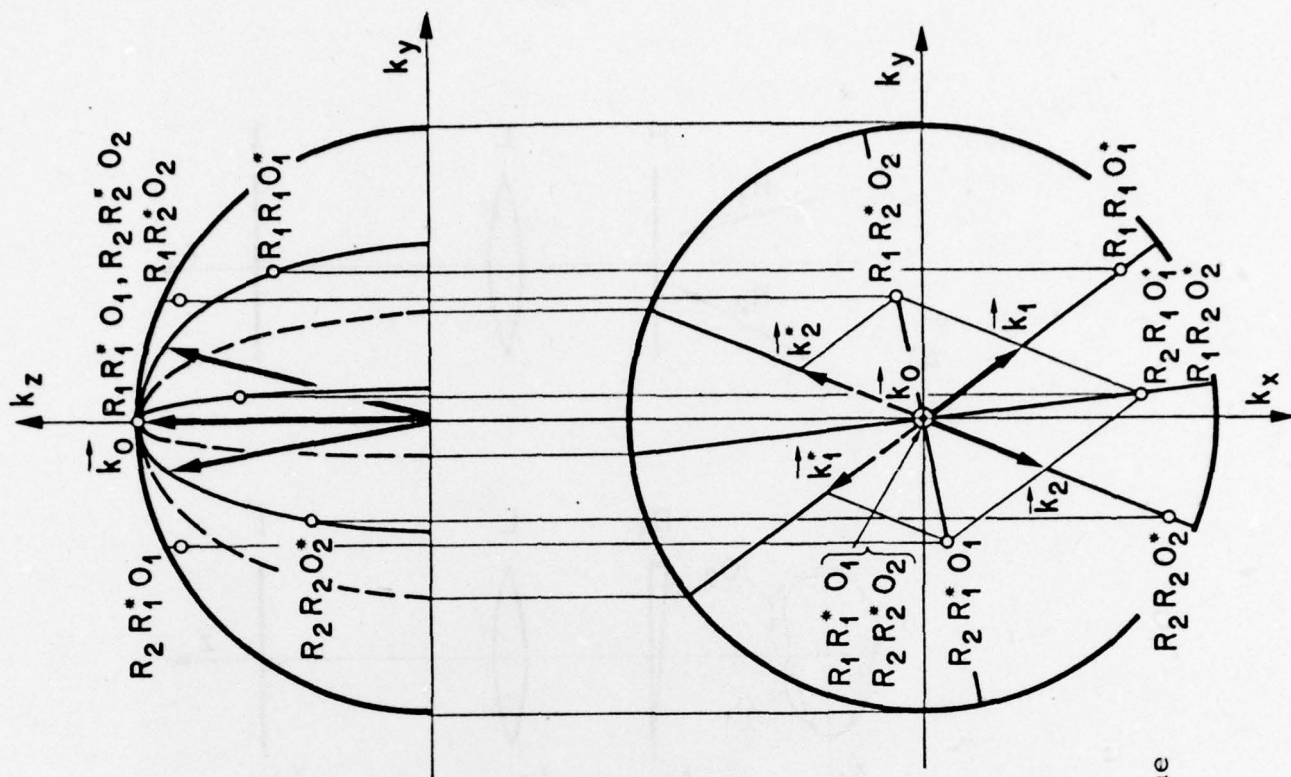
Fig. 2.4 Propagation directions associated with various reconstructed images are marked as points on the surface of the k sphere. The wavevectors of the object and reference waves are $\vec{k}_o$, $\vec{k}_1$, and $\vec{k}_2$, respectively.
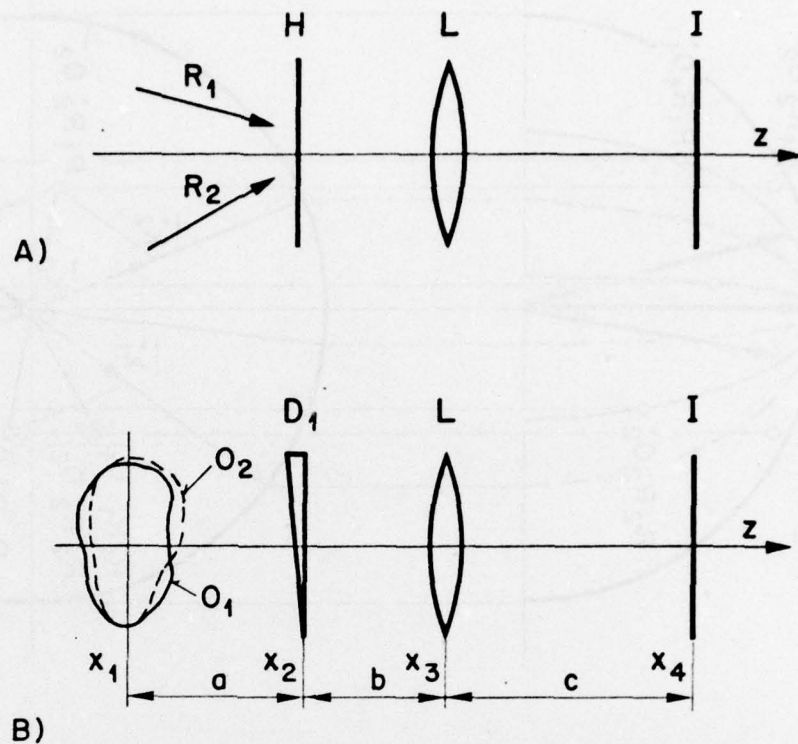
Fig. 2.5 Schematic arrangement for evaluating misalignment fringe effects on the interference pattern. (A) O_1 and O_2 are reconstructed from the hologram H by their respective reference waves R_1 and R_2. (B) Misalignment of R_1 is subst[i]tuted by a wedge D_1 in the hologram plane H acting on O_1 only.
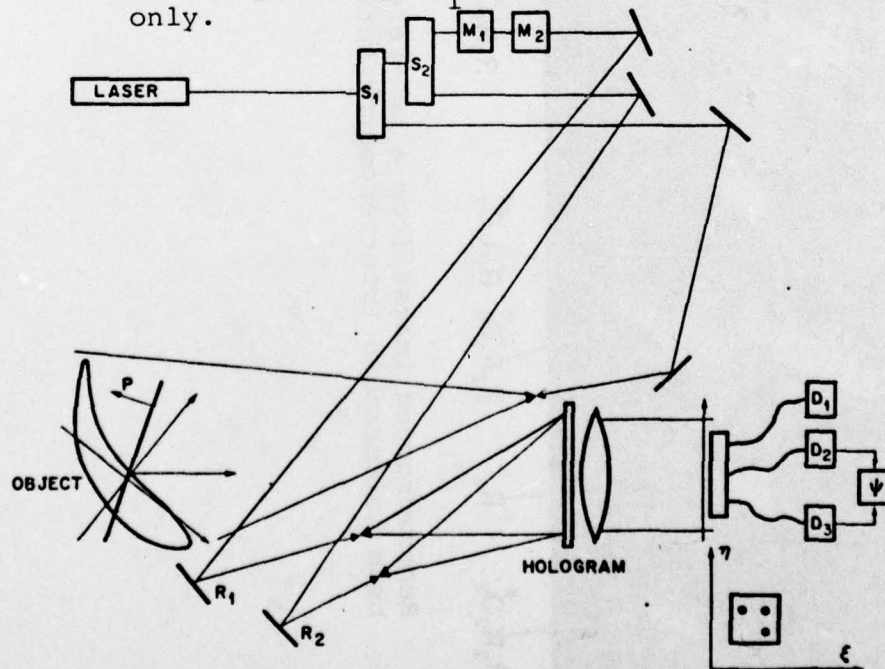
Fig. 2.6 Setup for heterodyne holographic interferometry: beam splitters S, acoustooptical modulators M, detectors D, image plane (ξ, η)
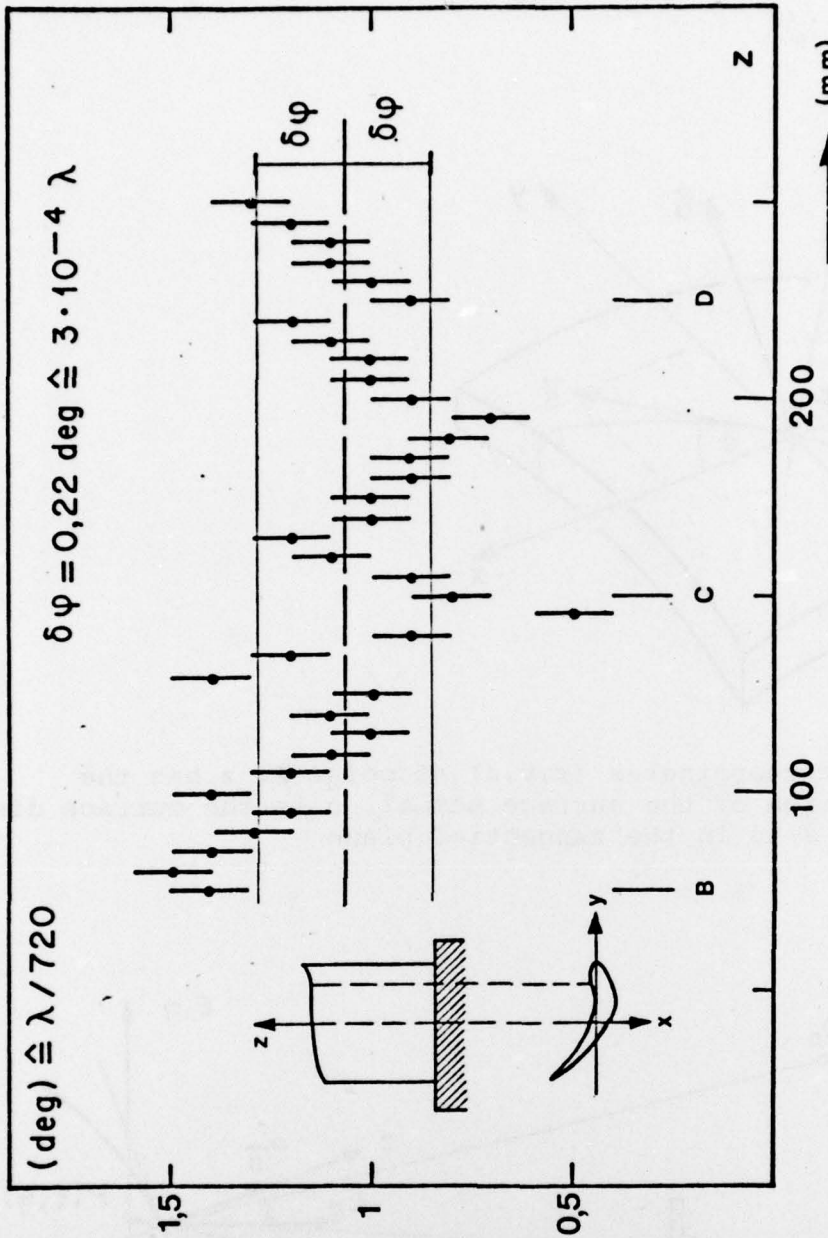
Fig. 2.8   Accuracy δφ of interference phase measurement determined from the measured phase along an undeformed object.

Fig. 2.7   Electronic equipment for heterodyne holographic interfero-metry. From top to bottom: X-Y control unit for detector position in image plane (ξ,η), dual phasemeter measuring Δφξ and Δφη, regulated power supplies for the photomulti-pliers and input filters, tape puncher for output data, acoustooptical modulator driver.
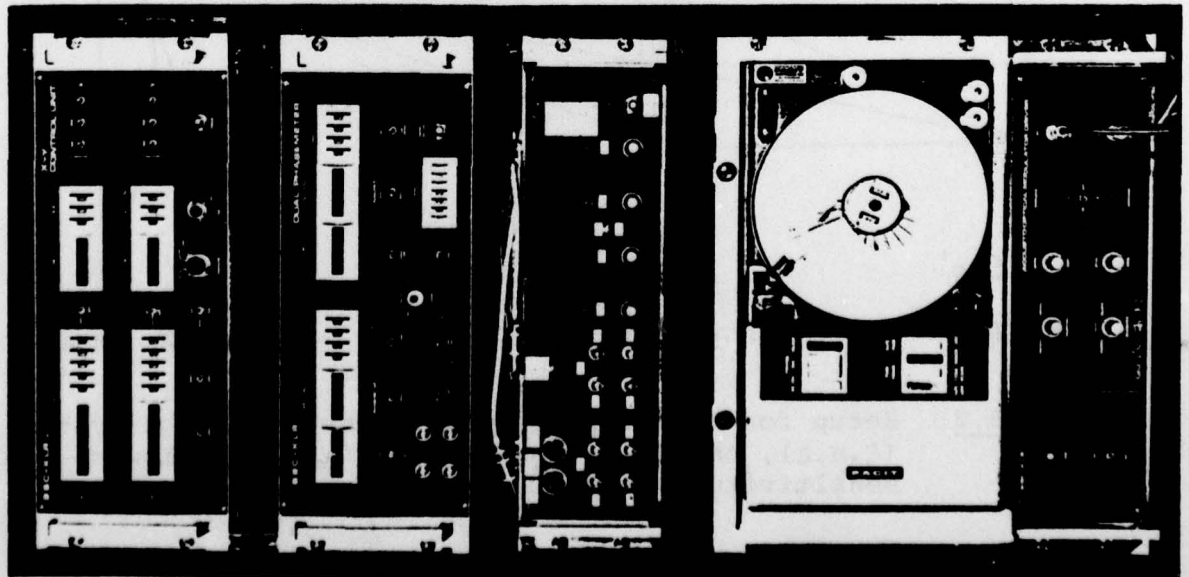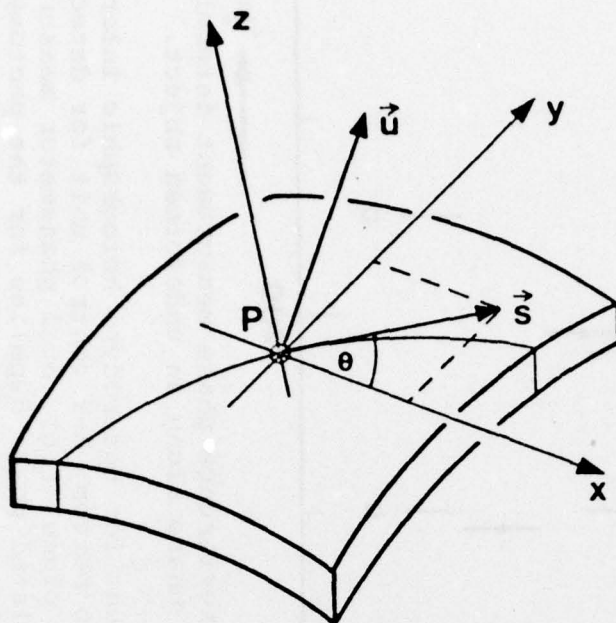
Fig. 3.1   Object coordinates (x,y,z) at point P: z has the
direction of the surface normal, $\vec{u}$ is the surface displace-
ment, $\vec{s}$ is in the tangential plane
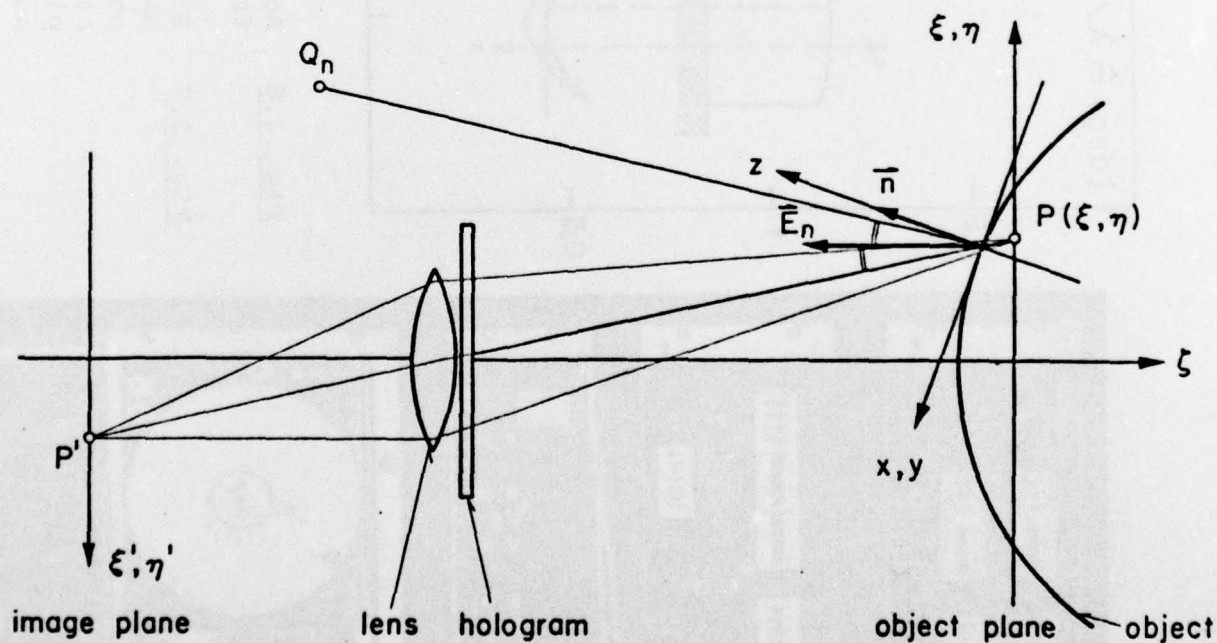
Fig. 3.2   Setup for holographic interferometry: image system
(ξ,η,ζ), object system (x,y,z), illumination sources O_n,
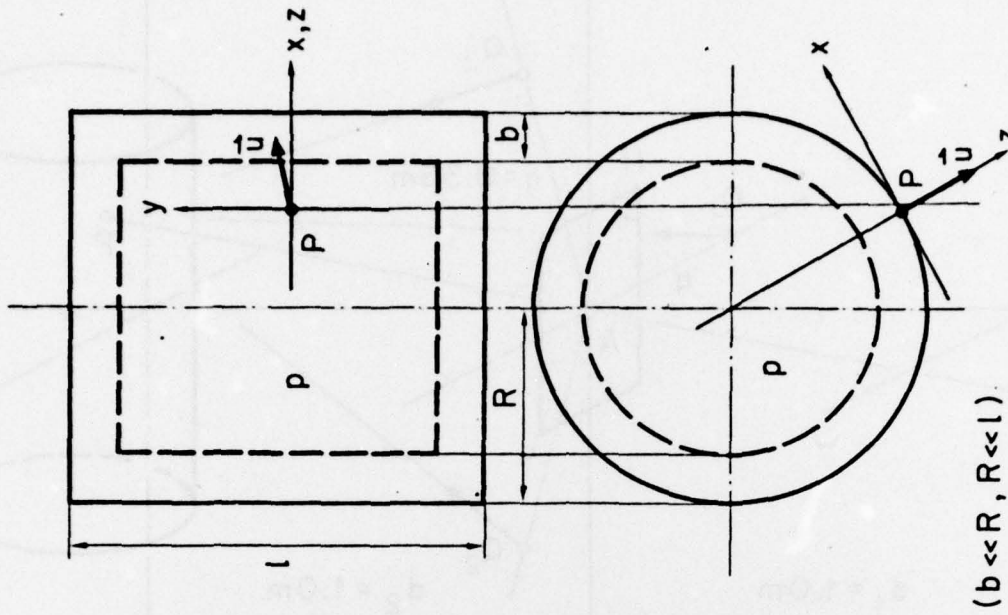sensitivity vectors $\vec{E}_n(\xi,\eta)$.

Fig. 3.4 Test object: cylindrical tube with internal pressure p. Surface displacement u at point P.

$(b \ll R, R \ll l)$.
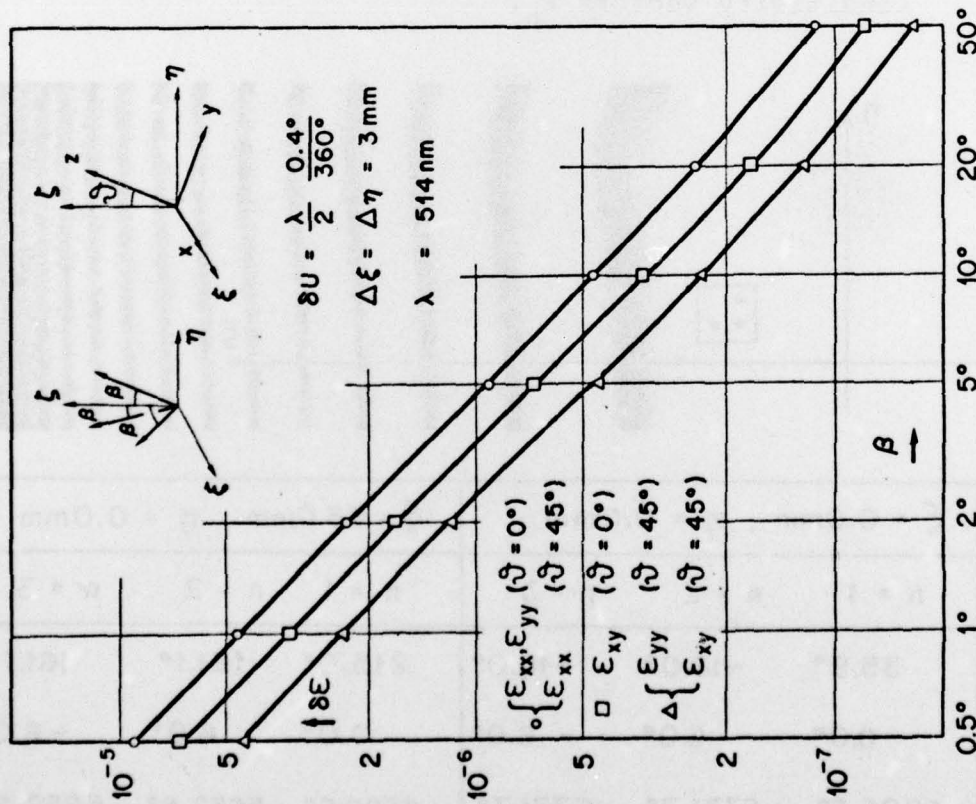

Fig. 3.3 Sensitivity $\delta\varepsilon$ for in-plane strain measurement. β angle between sensitivity vectors $\vec{\xi}$ and $\vec{\zeta}$, ϑ tilt of surface normal, $\Delta\xi = \Delta\eta$ spatial resolution, δU measuring error corresponding to 0.4° phase accuracy.
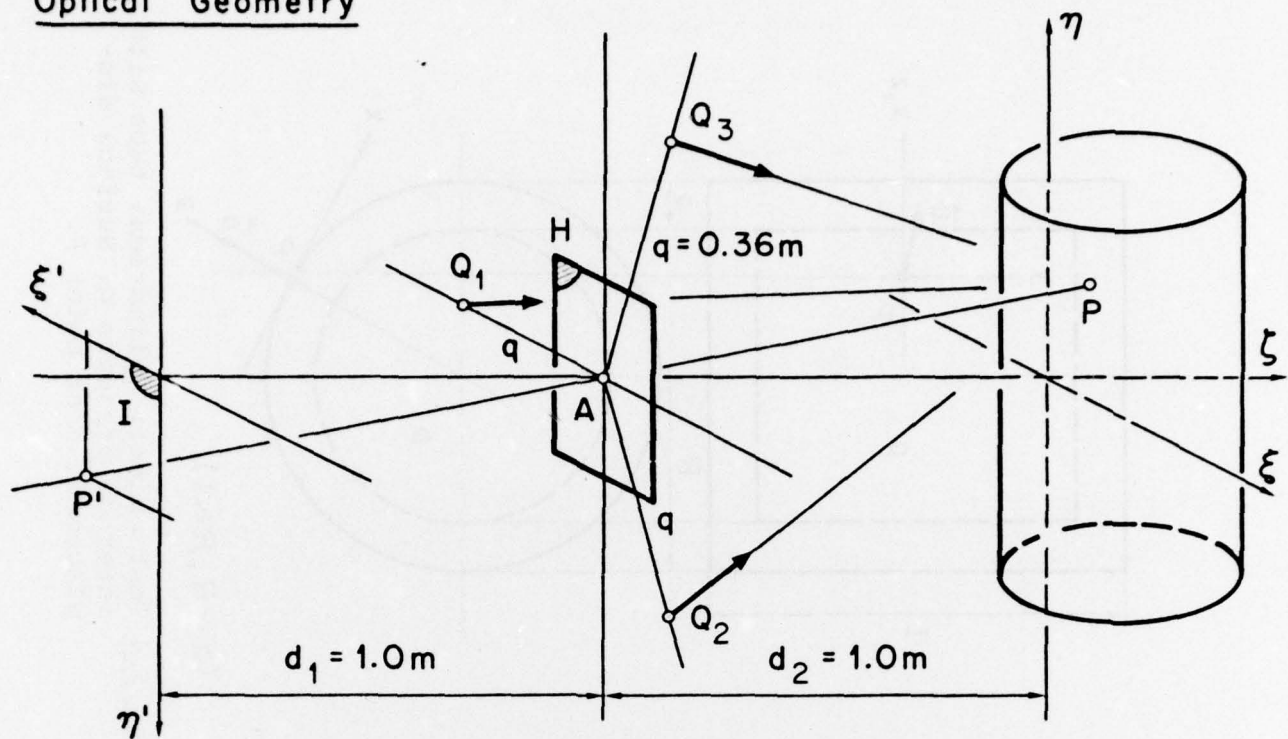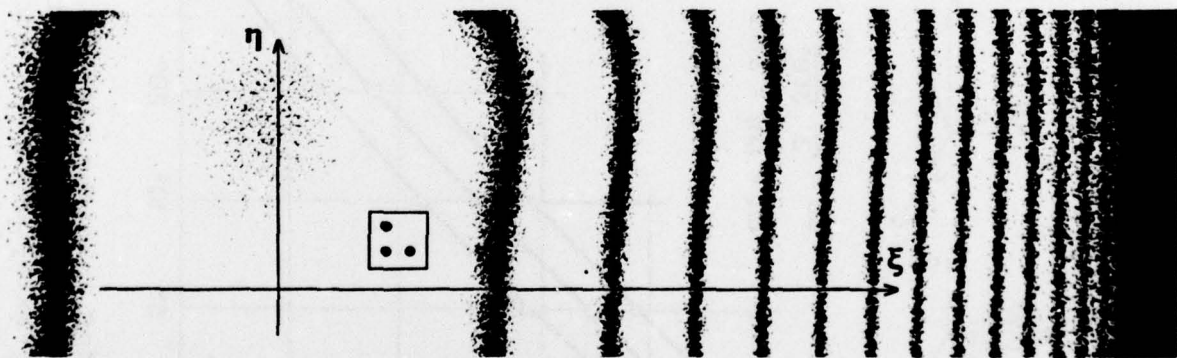
Optical Geometry

Fig. 3.5   Optical geometry for holographic strain measurement of the test object. Illumination sources Q_1, Q_2, Q_3 for three consecutive hologram recordings with different sensitivity vectors $\vec{E}_n$.

| $\Delta\xi$=3mm	$\xi = 0.0$mm , $\eta = 0.0$mm			$\xi = 66.0$mm , $\eta = 0.0$mm		
$\Delta\eta$=3mm	n = 1	n = 2	n = 3	n = 1	n = 2	n = 3
$\Delta_\xi\varphi_n$	35.9°	-18.0°	-18.0°	215.0°	161.1°	161.1°
$\Delta_\eta\varphi_n$	0.0°	6.0°	- 6.0°	0.0°	6.0°	-6.0°
φ_{on}	-6825.6°	-6771.7°	-6771.7°	-4520.6°	-5652.5°	-5652.5°

Fig. 3.6   Expected fringe pattern with detector array and simulated phase measurement for the test object.
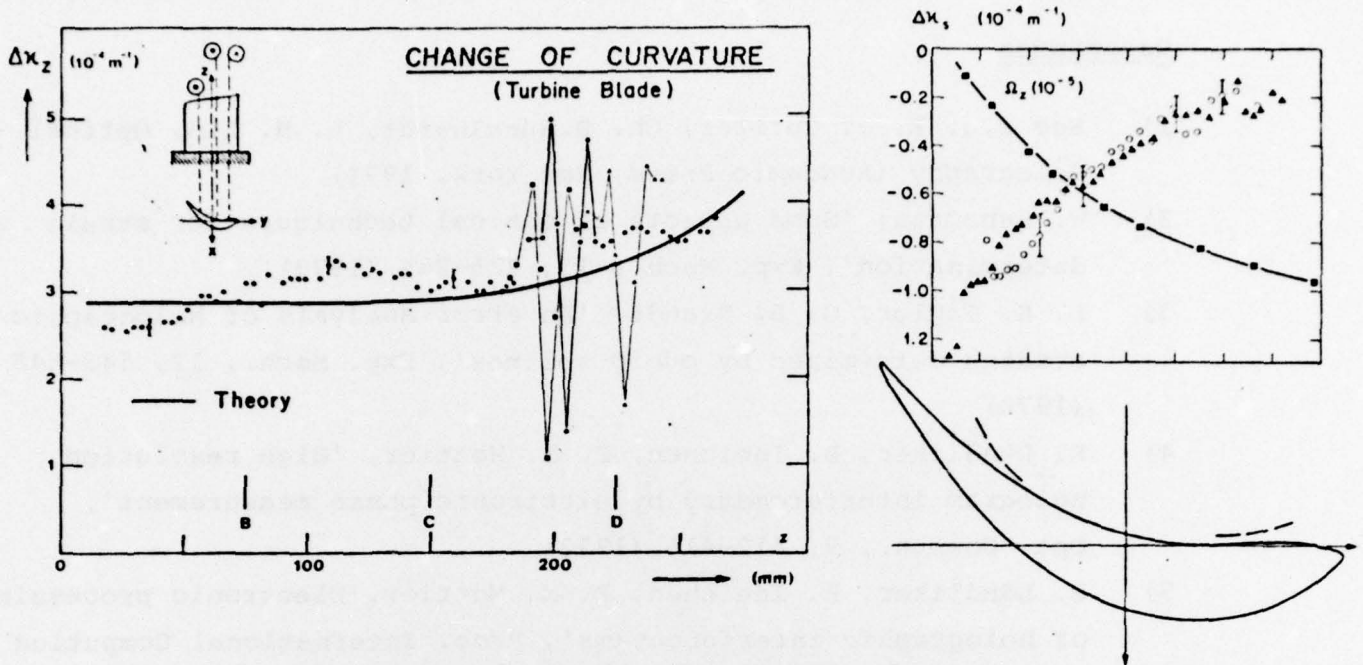
Fig. 3.7   Experimental results for pure bending of
a turbine blade under static load
a) Bending $\Delta\kappa_z$ along blade axis z. The local devations
around z = 200 mm appear reproducibly at different
positions within the blade profile
b) Change of curvature $\Delta\kappa_s$ and tilt Ω_z of the cross-section.
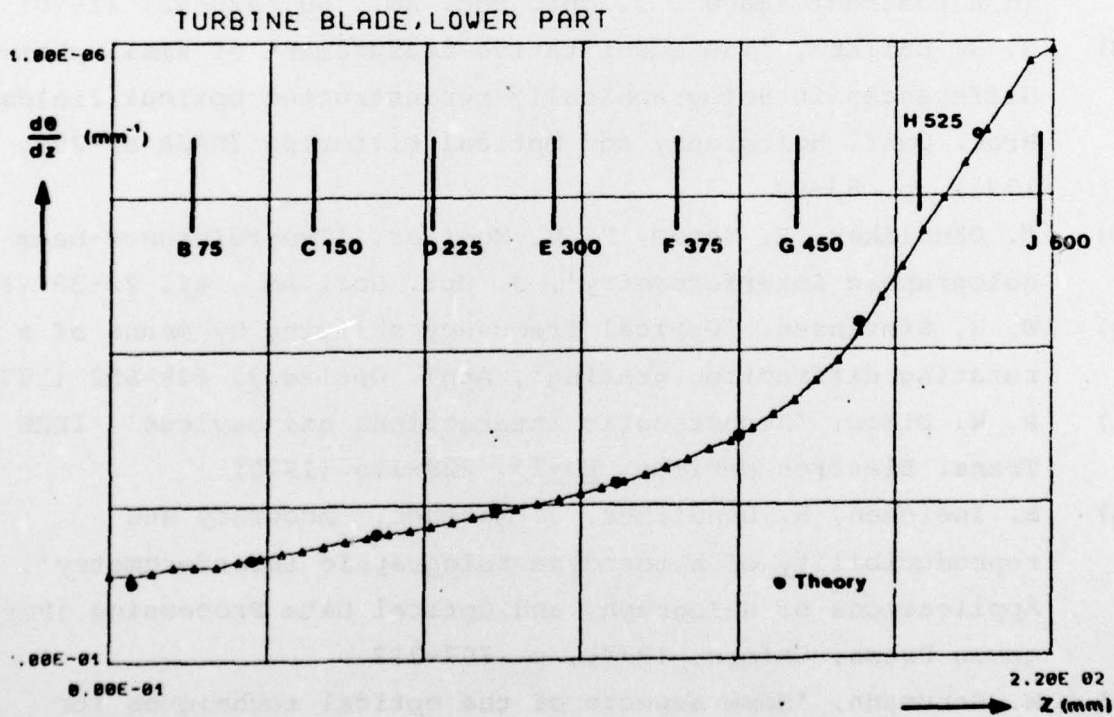
Fig. 3.8   Experimental results for pure torsion $d\theta/dz$ of a
turbine blade around blade axis z compared with theory.

References

1) See e.g. R. J. Collier, Ch. B. Burckhardt, L. H. Lin, Optical Holography (Academic Press, New York, 1971)

2) W. Schumann, 'Some aspects of optical techniques for strain determination', Exp. Mech., 13, 225-231 (1973)

3) L. H. Taylor, G. B. Brandt, 'An error analysis of holographic strains determined by cubic splines', Exp. Mech., 12, 543-548 (1972)

4) R. Dändliker, B. Ineichen, F. M. Mottier, 'High resolution hologram interferometry by electronic phase measurement', Opt. Commun., 9, 412-416 (1973)

5) R. Dändliker, B. Ineichen, F. M. Mottier, 'Electronic processing of holographic interferograms', Proc. International Computing Conference (IEEE Inc., New York, 1974), p. 69-72

6) R. Crane, 'New developments in interferometry. V. Interference phase measurement', Appl. Optics, 8, 538-542 (1969)

7) M. J. Dentino, C. W. Barnes, 'Measurement of complex amplitude in a coherent image', J. Opt. Soc. Am., 60, 420-421 (1970)

8) G. S. Ballard, 'The quantitative measurement of small phase differences in holographically reconstructed optical fields', Proc. Conf. Holography and Optical Filtering (NASA SP-299, 1971), p. 83-92

9) R. Dändliker, E. Marom, F. M. Mottier, 'Two-reference-beam holographic interferometry', J. Opt. Soc. Am., 66, 23-30 (1976)

10) W. H. Stevensen, 'Optical frequency shifting by means of a rotating diffraction grating', Appl. Optics, 9, 649-652 (1970)

11) R. W. Dixon, 'Acoustooptic interactions and devices', IEEE Trans. Electron Devices, ED-17, 229-235 (1970)

12) B. Ineichen, R. Dändliker, J. Mastner, 'Accuracy and reproducibility of heterodyne holographic interferometry', Applications of Holography and Optical Data Processing (Pergamon Press, Oxford, 1977), p. 207-212

13) W. Schumann, 'Some aspects of the optical techniques for strain determination', Exp. Mech., 13, 225-231 (1973)

14) R. Dändliker, B. Eliasson, B. Ineichen, F. M. Mottier, 'Quantitative determination of bending and torsion through holographic interferometry', The Engineering Uses of Coherent Optics, (Cambridge University Press, Cambridge, 1976), p. 99-117

15) A. Duschek, Vorlesungen über höhere Mathematik, Zweiter Band, (Springer-Verlag, Wien, 1963), p. 345-361

16) J. E. Sollid, 'Holographic interferometry applied to measurements of small static displacement of diffusely reflecting surfaces', Appl. Optics, 8, 1587-1595 (1969)

17) D. Bijl, R. Jones, 'A new theory for the practical interpretation of holographic interference patterns resulting from static surface displacements', Optica Acta, 21, 105-118 (1974)

18) S. K. Dhir, J. P. Sikora, 'An improved method for obtaining the general displacement field from a holographic interferogram', Exp. Mech., 12, 323-327 (1973)

19) R. Pryputniewicz, K. A. Stetson, 'Holographic strain analysis: Extension of fringe vector method to include perspective', Appl. Optics, 15, 725-728 (1976)

20) L. Ek, K. Biedermann, 'Analysis of a system for hologram interferometry with a continuously scanning reconstruction beam', Appl. Optics, 16, 2535-2542 (1977)

21) I. Szabo, Höhere Technische Mechanik, (Springer-Verlag, Berlin, 1964), p. 160-165

22) R. Dändliker, 'Quantitative strain measurement through holographic interferometry', Applications of Holography and Optical Data Processing (Pergamon Press, Oxford, 1977), p. 169-181